PERGAMON

International Journal of Solids and Structures 38 (2001) 3647–3672

INTERNATIONAL JOURNAL OF SOLIDS and STRUCTURES

www.elsevier.com/locate/ijsolstr

Plane strain finite element analysis of pressure sensitive plasticity with strong discontinuity

Richard A. Regueiro [a,*], Ronaldo I. Borja [b]

[a] *Center for Materials and Engineering Sciences, Sandia National Laboratories, P.O. Box 969, MS 9405, Livermore, CA 94551-0969, USA*

[b] *Department of Civil and Environmental Engineering, Stanford University, Stanford, CA 94305-4020, USA*

Received 6 June 2000

Abstract

Numerical simulations of localized deformation in solids should capture the structural phenomenon of localization and associated loss of material body strength in a manner independent of spatial discretization. Many regularization techniques have been proposed to address the ill posedness associated with rate-independent softening plasticity that leads to mesh-dependent numerical simulations. One approach to alleviating mesh dependence is the strong discontinuity approach, which represents localized deformation as a slip surface within a plasticity model; a strong discontinuity is a discontinuous displacement field. This approach is used in this paper to formulate a plane strain, pressure sensitive, nonassociative plasticity model with strong discontinuity and to implement the model, along with an enhanced bilinear quadrilateral element, via an assumed enhanced strain method. Numerical examples demonstrate mesh independence of the method for pressure sensitive materials.

Keywords: Localized deformation; Geomaterials; Failure model; Strong discontinuity; Pressure sensitive nonassociative plasticity; Assumed enhanced strain finite element method

1. Introduction

Geomaterials such as rock, heavily overconsolidated clays, or dense sands commonly exhibit localized deformation. In practice, limit-equilibrium-type analyses (Janbu, 1954; Enger, 1971) are still conducted to conservatively predict potential instability in earthen structures constructed from these types of geomaterials, such as top–down sequential excavations performed for almost any new building construction. Although such analyses are useful for designing relatively simple earthen structures, more sophisticated numerical methods like the finite element method are becoming necessary for analyzing complex designs. Applications of interest requiring such sophisticated numerical methods include extraction of oil and natural gas from deep underground reservoirs as well as deep underground construction associated with

* Corresponding author. Tel.: +1-925-294-4745; fax: +1-925-294-3410.
E-mail address: raregue@sandia.gov (R.A. Regueiro).

0020-7683/01/$ - see front matter
PII: S0020-7683(00)00250-X

nuclear waste repositories and the strategic petroleum reserve, which stores a large reserve of crude oil for national emergency purposes.

Localized deformation in geomaterials has been studied extensively to understand its inception and evolution from a microscopic perspective in order to describe the observed phenomenological/macroscopic behavior (e.g., acoustic imaging by Holcomb and Costin (1986) and DiGiovanni et al. (2000)). Microscale experimentation and imaging is useful for understanding the underlying physics of the observed phenomena (Fredrich, 1999) and essential when modeling material bodies on the order of nanometers to millimeters in size. For larger scales of interest (i.e., centimeters to meters, and meters to kilometers, depending on the material and application), physically-based internal state variable constitutive models (Rice, 1971; Lubliner, 1990; Bammann, 2001) which capture the macroscopic effect of the microscopic mechanisms are used. From this perspective, this paper presents an internal state variable model that accounts for the 'fine scale' agents which lead to macroscopic localized deformation in geomaterials (Garikipati and Hughes, 2000b). In short, this paper presents a phenomenological approach to modeling localized deformation in geomaterials via a strong discontinuity plasticity model implemented within an enhanced strain finite element framework.

Associated with the appearance of localized deformation is the loss of material body strength. In the past, rate-independent strain-softening plasticity models have been used to represent this 'softening' behavior in geomaterials (Prevost and Höeg, 1975). A significant drawback associated with these models is that they lead to mesh-dependent finite element solutions because such models do not contain an intrinsic material length scale needed to define the width of a localized deformation zone and because the resulting governing partial differential equation (PDE) is ill posed (Sandler and Wright, 1984). It has also been shown that mesh alignment of standard finite elements affects the simulated localized deformation pattern.

In the absence of an intrinsic material 'length scale', adaptive remeshing, or another regularization technique (e.g., viscous regularization), rate-independent softening plasticity models do not lead to finite element solutions that satisfy two necessary criteria for the solution to be meaningful (i.e., mesh-independent): objectivity with respect to mesh refinement and insensitivity to mesh alignment. Rate-dependent plasticity models contain an intrinsic length scale that regularizes the mesh pathology associated with the rate-independent limit, while generating a well-posed governing PDE (Sandler and Wright, 1984; Needleman, 1988; Loret and Prevost, 1990). Here, though it is of interest to consider the rate-independent case directly since many geomechanical initial boundary value problems entail loading rates slow enough such that the rate-independent limit is appropriate. It is noted here for completeness that rate-dependent plasticity with strong discontinuity has been addressed for $J2$ flow and thus allows representation of localized deformation via such models (Armero, 1999). Other models which contain an intrinsic length scale are the higher-order gradient plasticity models (Aifantis, 1984; de Borst and Pamin, 1996; Ramaswamy and Aravas, 1998a,b; Bammanni et al., 1999) and the micropolar continuum models (Cosserat and Cosserat, 1909; Mindlin, 1963; de Borst and Sluys, 1991). A variational multiscale method has been developed which provides a general framework for implementing such multiscale material models, whereby the finite element mesh does not need to be refined to the size of the material length scale in order to achieve a mesh-independent solution (Hughes, 1995; Hughes et al., 1998; Garikipati and Hughes, 1998, 2000a).

A recently developed phenomenological model (Regueiro and Borja, 1999; Borja and Regueiro, 2001) extends the strong discontinuity approach developed by Simo and co-workers (Simo et al., 1993; Simo and Oliver, 1994; Armero and Garikipati, 1995, 1996; Oliver et al., 1999) to pressure sensitive, nonassociative plasticity models. The strong discontinuity approach yields mesh-independent finite element solutions without introducing a material length scale and without requiring special mesh alignment strategies. The finite element solutions are objective with respect to mesh refinement because dissipation is calculated over a set of zero measure (a surface) and, as a result, is independent of finite element diameter (Simo et al., 1993; Regueiro and Borja, 1999). The finite element solutions are insensitive to mesh alignment because the slip surface orientation is embedded within the finite element (along with the slip surface constitutive relation)

via the assumed enhanced strain method (Simo and Rifai, 1990; Armero and Garikipati, 1995). In addition, by generating mesh-independent finite element solutions of localized deformation, the strong discontinuity approach improves convergence characteristics of its Newton–Raphson iterative solution algorithm (i.e., quadratic convergence). This paper presents some recent advances made to the pressure sensitive, nonassociative model: (1) the plane-strain localization condition is determined in closed-form from $\det \boldsymbol{A} = 0$, where $\boldsymbol{A}$ is the nonsymmetric (no major symmetry) elastic-"perfectly"-plastic acoustic tensor defined in Eq. (14) (Borja and Regueiro, 2001), (2) separate post-bifurcation constitutive relations are proposed to govern the stress–displacement response along the discontinuity surface (Borja and Regueiro, 2001), and (3) proper algorithmic loading and unloading conditions are defined for post-localization behavior (this paper). The following restrictions are placed on the formulation and implementation: small deformations and rotations, drained condition (i.e., effect of pore-fluid influence is neglected), and quasi-static, isothermal loading.

A summary of symbolic notation used throughout this paper is noted here. Boldface denotes tensors, i.e., $(\boldsymbol{a})_{ij} = a_{ij}$. The symmetric dyadic product in index notation is $(\boldsymbol{a} \otimes \boldsymbol{b})^{\mathrm{s}}_{ij} = \frac{1}{2}(a_i b_j + a_j b_i)$, where the superscript "s" denotes a symmetric second-order tensor which belongs to the space of real symmetric second-order tensors $\mathbb{S}$. The dot product is expressed as $\boldsymbol{a} \cdot \boldsymbol{b} = a_i b_i$, where Einstein's summation convention is used. The inner product symbol ":" is used for contraction of two second-order tensors as $\boldsymbol{a} : \boldsymbol{b} = a_{ij} b_{ij}$ or for the contraction of a fourth-order tensor and a second-order tensor as $\boldsymbol{c} : \boldsymbol{a} = c_{ijkl} a_{kl}$. The divergence operator acting on a second-order tensor is written as $(\boldsymbol{\nabla} \cdot \boldsymbol{a})_i = a_{ij,j}$, where the comma denotes partial differentiation with respect to x_j. The symmetric gradient operator acting on a vector is written as $(\boldsymbol{\nabla}^{\mathrm{s}} \boldsymbol{a})_{ij} = \frac{1}{2}(a_{i,j} + a_{j,i})$. The Euclidean norm of a second-order tensor is written as $\|\boldsymbol{a}\| = \sqrt{a_{ij} a_{ij}}$. The partial differential operator $\partial_{\boldsymbol{a}} \phi$ denotes $\partial \phi / \partial \boldsymbol{a}$, or $\partial_{a_{ij}} \phi = \partial \phi / \partial a_{ij}$. The trace operator is $\mathrm{tr}(\boldsymbol{a}) = a_{ii}$.

2. Governing equations with discontinuity

Consider a closed body $\overline{\Omega} \subset \mathbb{R}^{n_{\mathrm{dim}}}$ ($n_{\mathrm{dim}} = 1, 2, \text{or } 3$) with smooth (i.e., C^1) internal discontinuity surface $\mathscr{S} \subset \mathbb{R}^{n_{\mathrm{dim}}-1}$ as shown in Fig. 1. Let $\boldsymbol{x} \in \Omega$ denote the location of material particles $\boldsymbol{x}$ in Ω.

The local form of quasi-static, isothermal equilibrium is written as follows (Hughes, 1987): Given $\boldsymbol{b} : \Omega \to \mathbb{R}^{n_{\mathrm{dim}}}$, $\boldsymbol{t}^{\sigma} : \Gamma_t \to \mathbb{R}^{n_{\mathrm{dim}}}$, and $\boldsymbol{g} : \Gamma_u \to \mathbb{R}^{n_{\mathrm{dim}}}$, find $\boldsymbol{u} : \overline{\Omega} \times [0, T] \to \mathbb{R}^{n_{\mathrm{dim}}}$ (where $[0, T] \subset \mathbb{R}_+$ is the time interval of interest) such that

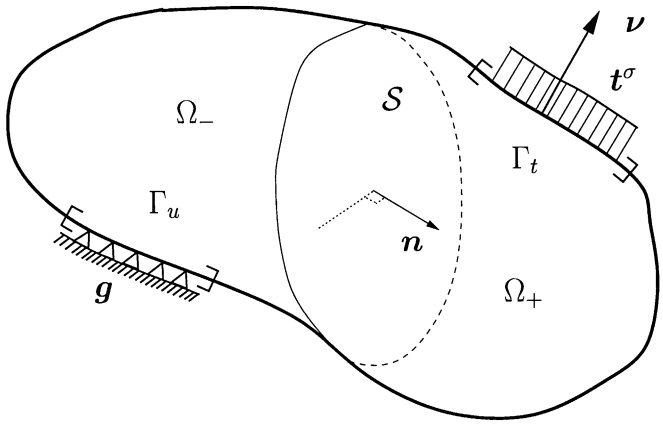

Fig. 1. Body $\overline{\Omega}$ with discontinuity $\mathscr{S}(\Omega = \Omega_+ \cup \Omega_-, \partial\Omega = \Gamma_t \cup \Gamma_u \cup \mathscr{S},\ \overline{\Omega} = \Omega \cup \partial\Omega)$.

$$\begin{aligned} \nabla \cdot \boldsymbol{\sigma} + \boldsymbol{b} &= \boldsymbol{0} \quad \text{in } \Omega, \\ \boldsymbol{\sigma} \cdot \boldsymbol{v} &= \boldsymbol{t}^{\sigma} \quad \text{on } \Gamma_t, \\ \boldsymbol{u} &= \boldsymbol{g} \quad \text{on } \Gamma_u, \\ [\![\boldsymbol{\sigma}]\!] \cdot \boldsymbol{n} = [\![\boldsymbol{t}^{\sigma}_{\mathscr{S}}]\!] &= \boldsymbol{0} \quad \text{across } \mathscr{S}, \end{aligned} \tag{1}$$

where $\boldsymbol{\sigma}$ is the Cauchy stress, $\boldsymbol{b}$, the prescribed body force, $\boldsymbol{v}$, the unit normal to Γ_t, $\boldsymbol{n}$, the unit normal to $\mathscr{S}$, $\boldsymbol{t}^{\sigma}$, the prescribed traction, $\boldsymbol{g}$, the prescribed displacement, and $[\![\bullet]\!]$ denotes the jump of a quantity across $\mathscr{S}$ (i.e., $[\![\boldsymbol{\sigma}]\!] = \boldsymbol{\sigma}^{+} - \boldsymbol{\sigma}^{-}$).

The variational form of quasi-static equilibrium, using the local form as a point of departure, may be written as follows (Hughes, 1987): Given $\boldsymbol{b} : \Omega \to \mathbb{R}^{n_{\text{dim}}}$, $\boldsymbol{t}^{\sigma} : \Gamma_t \to \boldsymbol{R}^{n_{\text{dim}}}$, and $\boldsymbol{g} : \Gamma_u \to \mathbb{R}^{n_{\text{dim}}}$, find $\boldsymbol{u} \in \mathscr{U}$ such that for all $\boldsymbol{\eta} \in \mathscr{V}$,

$$\int_{\Omega} \nabla^{\text{s}} \boldsymbol{\eta} : \boldsymbol{\sigma} \, \mathrm{d}\Omega = \int_{\Omega} \boldsymbol{\eta} \cdot \boldsymbol{b} \, \mathrm{d}\Omega + \int_{\Gamma_t} \boldsymbol{\eta} \cdot \boldsymbol{t}^{\sigma} \, \mathrm{d}\Gamma + \int_{\mathscr{S}} \boldsymbol{\eta} \cdot ([\![\boldsymbol{\sigma}]\!] \cdot \boldsymbol{n}) \mathrm{d}\Gamma, \tag{2}$$

where $\boldsymbol{\eta} = \delta \boldsymbol{u}$ is the weighting function and first variation of $\boldsymbol{u}$. The space of admissible weighting functions is defined as

$$\mathscr{V} := \left\{ \boldsymbol{\eta} : \Omega \to \mathbb{R}^{n_{\text{dim}}} | \boldsymbol{\eta} \in H^1 | \boldsymbol{\eta} = \boldsymbol{0} \text{ on } \Gamma_u \right\}, \tag{3}$$

and the space of admissible trial solutions is defined as

$$\mathscr{U} := \left\{ \boldsymbol{u} : \overline{\Omega} \to \mathbb{R}^{n_{\text{dim}}} | \boldsymbol{u} \in H^1 | \boldsymbol{u} = \boldsymbol{g} \text{ on } \Gamma_u \right\}, \tag{4}$$

where H^1 is the first Sobolev space.

3. Kinematics of strong discontinuities

For rate-independent, infinitesimal, perfect plasticity, discontinuous displacement fields are admissible solutions to the boundary value problem and are contained within a solution space called the bounded deformation (BD) space (Matthies et al., 1979). The infinitesimal strains are singular distributions and are contained within the space of bounded measures because the integral of the Dirac-delta function is a finite measure. The discontinuous displacement field is defined as

$$\boldsymbol{u}(\boldsymbol{x}, t) := \underbrace{\overline{\boldsymbol{u}}(\boldsymbol{x}, t)}_{\text{continuous}} + \underbrace{[\![\boldsymbol{u}(t)]\!] H_{\mathscr{S}}(\boldsymbol{x})}_{\text{discontinuous}}, \tag{5}$$

where $[\![\boldsymbol{u}(t)]\!] = \boldsymbol{u}^{+} - \boldsymbol{u}^{-} = \zeta(t)\boldsymbol{m}$ is the jump in displacement across the discontinuity surface $\mathscr{S}$ and is assumed independent of $\boldsymbol{x}$, $\zeta(t)$, the jump magnitude dependent on time t, $\boldsymbol{m}$, the unit vector designating the jump direction, and $H_{\mathscr{S}}(\boldsymbol{x})$, the Heaviside function defined as

$$H_{\mathscr{S}}(\boldsymbol{x}) = \begin{cases} 1 & \text{if } \boldsymbol{x} \in \Omega_{+}, \\ 0 & \text{if } \boldsymbol{x} \in \Omega_{-}. \end{cases} \tag{6}$$

The jump displacement $[\![\boldsymbol{u}(t)]\!]$ could vary spatially along the discontinuity $\mathscr{S}$ (i.e., $[\![\boldsymbol{u}(\boldsymbol{x}, t)]\!]$), but for simplicity here it is considered spatially invariant. The symmetric gradient of the displacement field in Eq. (5), treating the Dirac-delta function as a distribution, is the small strain tensor (Simo et al., 1993)

$$\boldsymbol{\epsilon}(\boldsymbol{x}, t) := \nabla^{\text{s}} \boldsymbol{u} = \underbrace{\nabla^{\text{s}} \overline{\boldsymbol{u}}(\boldsymbol{x}, t) + \underbrace{\nabla^{\text{s}} [\![\boldsymbol{u}(t)]\!]}_{=\boldsymbol{0}} H_{\mathscr{S}}(\boldsymbol{x})}_{\text{regular}} + \underbrace{([\![\boldsymbol{u}(t)]\!] \otimes \boldsymbol{n})^{\text{s}} \delta_{\mathscr{S}}(\boldsymbol{x})}_{\text{singular}}, \tag{7}$$

where $\boldsymbol{n}$ is the unit normal to the discontinuity surface $\mathscr{S}$ pointing into Ω_+ (Fig. 1), and $\delta_{\mathscr{S}}$ is the Dirac-delta function on $\mathscr{S}$. Essentially, the gradient of the Heaviside function is $\nabla H_{\mathscr{S}} = \boldsymbol{n}\delta_{\mathscr{S}}$. The Dirac-delta function is treated in a distributional framework (Stakgold, 1998) throughout the formulation of a plasticity model with strong discontinuity.

4. Nonassociative pressure sensitive plasticity with strong discontinuity

Aspects of nonassociative pressure sensitive plasticity with strong discontinuity are discussed along with details for nonassociative Drucker–Prager plasticity formulated in the context of strong discontinuities.

4.1. Localized plastic deformation

A material body with discontinuous displacements (whose presence is detected by the localization condition in Eq. (14)) has singular strains at discontinuity $\mathscr{S}$ and plastic flow localized to $\mathscr{S}$ (Simo et al., 1993) that in turn results in a singular distribution plastic consistency parameter as

$$\lambda = \lambda_\delta \delta_{\mathscr{S}}. \tag{8}$$

Eq. (8) states that all further irrecoverable deformation occurs along the discontinuity $\mathscr{S}$ since plastic deformation is localized there. Thus, the evolution of the internal state variables is also localized to the discontinuity $\mathscr{S}$. For some geomaterials this is a gross approximation because irrecoverable deformation is not completely localized to a surface (e.g., granular materials that typically exhibit shear bands of finite width (Vardoulakis et al., 1978)). Thus, a shear-band-to-slip-surface transition would be more appropriate for certain geomaterials (Aydin and Johnson, 1983; Oliver et al., 1999). This transition will be considered in a future paper.

The stress rate $\dot{\boldsymbol{\sigma}}$ must be regular (Simo et al., 1993). From Regueiro and Borja (1999), $\dot{\boldsymbol{\sigma}}$ may be written as

$$\dot{\boldsymbol{\sigma}} = \boldsymbol{c}^{\mathrm{e}} : \nabla^{\mathrm{s}}\dot{\boldsymbol{u}} + \underbrace{\boldsymbol{c}^{\mathrm{e}} : \left[(\llbracket \dot{\boldsymbol{u}} \rrbracket \otimes \boldsymbol{n})^{\mathrm{s}} - \lambda_\delta \frac{\partial \varphi}{\partial \boldsymbol{\sigma}} \right]}_{=\mathbf{0}} \delta_{\mathscr{S}} \tag{9}$$

$$\Rightarrow \quad \dot{\boldsymbol{\sigma}} = \boldsymbol{c}^{\mathrm{e}} : \nabla^{\mathrm{s}}\dot{\boldsymbol{u}}, \tag{10}$$

where $\boldsymbol{c}^{\mathrm{e}}$ is the constant fourth-order tangent elastic modulus tensor and $\varphi(\boldsymbol{\sigma}, \alpha) : \mathbb{S} \times \mathbb{R} \to \mathbb{R}$ is the plastic potential function. Thus, the stress is calculated solely from the regular part of the strain field in Eq. (10). Note that the tensor coefficient of the singular part of the right-hand side of Eq. (9) must be zero in order for the stress rate $\dot{\boldsymbol{\sigma}}$ to be regular. The tensor contraction of $\boldsymbol{c}^{\mathrm{e}}$ (assuming isotropy) with the difference within the brackets in Eq. (9) implies that the two terms within the brackets are equal (i.e., $(\llbracket \dot{\boldsymbol{u}} \rrbracket \otimes \boldsymbol{n})^{\mathrm{s}} = \lambda_\delta \partial_{\boldsymbol{\sigma}} \varphi$). This would not be possible because there would be an inconsistency in rank. The tensor $(\llbracket \dot{\boldsymbol{u}} \rrbracket \otimes \boldsymbol{n})^{\mathrm{s}}$ is rank two because of its symmetry, while $\lambda_\delta \partial_{\boldsymbol{\sigma}} \varphi$ is rank three for general three-dimensional stress conditions. This result would inhibit the formation of discontinuous displacement fields unless a separate post-bifurcation plastic potential function $g(\boldsymbol{\sigma}, c)$ is assumed (Borja and Regueiro, 2001). Further discussion will follow in this paper.

4.2. Localization condition

In order to be able to detect the presence of discontinuous displacements, a localization condition is derived. When this condition is met, the solution bifurcates, allowing discontinuous displacements to

appear within the material body. Eq. (2) showed that for equilibrium to be satisfied, the traction must be continuous across the discontinuity surface $\mathscr{S}$:

$$[\![\dot{\boldsymbol{\sigma}}]\!] \cdot \boldsymbol{n} = [\![\dot{\boldsymbol{t}}^{\sigma}_{\mathscr{S}}]\!] = \boldsymbol{0}. \tag{11}$$

This condition – along with the requirement that the stress rate be regular – requires that the traction rate be regular. The traction rate is

$$\dot{\boldsymbol{t}}^{\sigma}_{\mathscr{S}} = \boldsymbol{n} \cdot \dot{\boldsymbol{\sigma}} = \boldsymbol{n} \cdot \boldsymbol{c}^{\mathrm{e}} : \nabla^{\mathrm{s}} \dot{\boldsymbol{u}} + \underbrace{\boldsymbol{n} \cdot \boldsymbol{C}^{\mathrm{ep}} : ([\![\dot{\boldsymbol{u}}]\!] \otimes \boldsymbol{n})^{\mathrm{s}}}_{=\boldsymbol{0}} \delta_{\mathscr{S}}, \tag{12}$$

where via the singular part of the consistency condition (Regueiro and Borja, 1999), $\boldsymbol{C}^{\mathrm{ep}}$ is expressed as

$$\boldsymbol{C}^{\mathrm{ep}} = \boldsymbol{c}^{\mathrm{e}} - \frac{\boldsymbol{c}^{\mathrm{e}} : \partial_{\boldsymbol{\sigma}} \varphi \otimes \partial_{\boldsymbol{\sigma}} \phi : \boldsymbol{c}^{\mathrm{e}}}{\partial_{\boldsymbol{\sigma}} \phi : \boldsymbol{c}^{\mathrm{e}} : \partial_{\boldsymbol{\sigma}} \varphi}, \tag{13}$$

and is called the elastic "perfectly"-plastic tangent modulus tensor, where $\phi(\boldsymbol{\sigma}, \alpha) : \mathbb{S} \times \mathbb{R} \to \mathbb{R}$ is the yield function. It is *perfectly* plastic because no hardening/softening parameter explicitly appears in the denominator of Eq. (13) as compared to a weak discontinuity formulation (Rudnicki and Rice, 1975). Note that $\boldsymbol{C}^{\mathrm{ep}}$ does not have major symmetry, which results from the nonassociative nature of the flow rule (i.e., $\partial_{\boldsymbol{\sigma}} \varphi \neq \partial_{\boldsymbol{\sigma}} \phi$). It has been shown that the governing partial differential equation resulting from nonassociative plasticity is ill posed (Schaeffer, 1990) which allows localization to be detected for a positive hardening/softening parameter, $H > 0$, in addition to $H \leqslant 0$ for associative plasticity. For the traction rate to be regular, the term before the Dirac-delta function in Eq. (12) must be zero, which leads to the localization condition in the following standard form:

$$\boldsymbol{A} \cdot \boldsymbol{m} = \boldsymbol{0} \quad \Rightarrow \quad \det \boldsymbol{A} = 0 \quad \text{for} \quad \boldsymbol{m} \neq \boldsymbol{0}, \tag{14}$$

where $\boldsymbol{A} = \boldsymbol{n} \cdot \boldsymbol{C}^{\mathrm{ep}} \cdot \boldsymbol{n}$ is the second-order elastic perfectly-plastic acoustic tensor. The localization condition $\det \boldsymbol{A} = 0$ may be solved numerically via a nonlinear optimization routine such as that described in Ortiz et al. (1987), or analytically for plane stress and plane strain as shown by Runesson et al. (1991). The analytical expression for plane strain will be delineated during the presentation of a nonassociative Drucker–Prager model.

4.3. Nonassociative Drucker–Prager plasticity

A simple nonassociative pressure sensitive plasticity model, the Drucker–Prager model, is now formulated in the context of strong discontinuities. It is appropriate for modeling the constitutive behavior of geomaterials but is limited in that it does not capture the difference in strength between triaxial compression and extension commonly observed for soils, nor does it satisfactorily describe a geomaterial's strength in the tension regime. Regardless of these limitations, because of its simplicity, nonassociative Drucker–Prager plasticity in the infinitesimal strain regime is useful for testing a new method like the strong discontinuity approach.

A quadratic stored energy density function $\Psi(\boldsymbol{\epsilon}^{\mathrm{e}}, \xi)$, which results in linear elasticity and linear hardening for an isothermal solid, is defined as

$$\Psi(\boldsymbol{\epsilon}^{\mathrm{e}}, \boldsymbol{\xi}) := \tfrac{1}{2} \boldsymbol{\epsilon}^{\mathrm{e}} : \boldsymbol{c}^{\mathrm{e}} : \boldsymbol{\epsilon}^{\mathrm{e}} + \tfrac{1}{2} H \xi^2, \tag{15}$$

where $\boldsymbol{c}^{\mathrm{e}}$ is the elastic modulus tensor, and H is the shear hardening/softening modulus. The fourth-order tensor $\boldsymbol{c}^{\mathrm{e}}$ is the isotropic elastic tangent modulus tensor defined as

$$\boldsymbol{c}^{\mathrm{e}} = \overline{\lambda} \boldsymbol{1} \otimes \boldsymbol{1} + 2\overline{\mu} \boldsymbol{I}, \tag{16}$$

where $\overline{\lambda}$ and $\overline{\mu}$ are the Lamé parameters, $(\mathbf{1})_{ij} = \delta_{ij}$ is the Kronecker-delta, and $(\boldsymbol{I})_{ijkl} = (\delta_{ik}\delta_{jl} + \delta_{il}\delta_{jk})/2$ is the fourth-order identity tensor.

Let the strain-like plastic internal variable $\xi : \Omega \times [0, T] \to \mathbb{R}$ be the deviatoric plastic strain measure e^{p}:

$$\xi := e^{\mathrm{p}} = \int_0^T \dot{e}^{\mathrm{p}}\,\mathrm{d}t, \tag{17}$$

where

$$\dot{v}^{\mathrm{p}} = \mathrm{tr}(\dot{\boldsymbol{\epsilon}}^{\mathrm{p}}), \qquad \dot{e}^{\mathrm{p}} = \sqrt{\frac{2}{3}}\|\dot{\boldsymbol{e}}^{\mathrm{p}}\|, \qquad \dot{\boldsymbol{e}}^{\mathrm{p}} = \dot{\boldsymbol{\epsilon}}^{\mathrm{p}} - (\dot{v}^{\mathrm{p}}/3)\mathbf{1}. \tag{18}$$

The stress-like plastic internal variable α is defined as

$$\alpha := -H\xi. \tag{19}$$

A Drucker–Prager yield function takes the form (Drucker and Prager, 1952)

$$\phi(\boldsymbol{\sigma}, \alpha) = \sqrt{\frac{3}{2}}\|\boldsymbol{s}\| + \sqrt{3}(\kappa + \beta p) = 0, \tag{20}$$

where

$$\boldsymbol{s} = \boldsymbol{\sigma} - p\mathbf{1}, \qquad \kappa := -\overline{\alpha} + \tfrac{1}{\sqrt{3}}\alpha, \qquad p = \tfrac{1}{3}\mathrm{tr}(\boldsymbol{\sigma}) \tag{21}$$

with derivatives

$$\frac{\partial\phi}{\partial\boldsymbol{\sigma}} = \sqrt{\frac{3}{2}}\hat{\boldsymbol{n}} + \frac{1}{\sqrt{3}}\beta\mathbf{1}, \qquad \frac{\partial\phi}{\partial\alpha} = 1, \tag{22}$$

and $\hat{\boldsymbol{n}} = \boldsymbol{s}/\|\boldsymbol{s}\|$. Continuum mechanics convention is used in this paper for which compression implies $p < 0$. The material constants $\overline{\alpha}$ and β are the cohesion-like strength parameter and friction-like parameter, respectively. A plastic potential function $\varphi(\boldsymbol{\sigma}, \alpha)$ is defined in a form similar to the yield function $\phi(\boldsymbol{\sigma}, \alpha)$ as

$$\varphi(\boldsymbol{\sigma}, \alpha) = \sqrt{\frac{3}{2}}\|\boldsymbol{s}\| + \sqrt{3}(\kappa + bp) \tag{23}$$

with derivatives

$$\frac{\partial\varphi}{\partial\boldsymbol{\sigma}} = \sqrt{\frac{3}{2}}\hat{\boldsymbol{n}} + \frac{1}{\sqrt{3}}b\mathbf{1}, \qquad \frac{\partial\varphi}{\partial\alpha} = 1, \tag{24}$$

where b is the material dilation constant. Note that associative plasticity results if $\beta = b$, but typically for geomaterials $\beta > b$ with $b > 0$ for a dilatant material and $b < 0$ for a contractant material. The $J2$ flow (von Mises) plasticity model is recovered when $\beta = b = 0$ which is appropriate for modeling the undrained condition in cohesive soil. The evolution equation for ξ is now

$$\dot{\xi} := \lambda\frac{\partial\varphi}{\partial\alpha} = \lambda, \quad \dot{e}^{\mathrm{p}} = \lambda, \tag{25}$$

where the evolution of plastic flow is $\dot{\boldsymbol{\epsilon}}^{\mathrm{p}} = \lambda\partial\varphi/\partial\boldsymbol{\sigma}$. Note that b takes the form

$$b = \frac{\dot{v}^{\mathrm{p}}}{\sqrt{3}\dot{e}^{\mathrm{p}}}, \tag{26}$$

which is analogous to the dilatancy factor used by Rudnicki and Rice (1975).

4.4. Localization condition for Drucker–Prager plasticity

For nonassociative Drucker–Prager plasticity with strong discontinuity the elastic-perfectly-plastic tangent modulus tensor results from Eq. (13) as

$$\boldsymbol{C}^{\mathrm{ep}} = \left(\overline{K} - \frac{2\overline{\mu}}{3} - \frac{3\beta b\overline{K}^2}{\chi}\right)\mathbf{1}\otimes\mathbf{1} + 2\overline{\mu}\boldsymbol{I} - \frac{6\overline{\mu}^2}{\chi}\hat{\boldsymbol{n}}\otimes\hat{\boldsymbol{n}} - \frac{3\sqrt{2}\overline{\mu}\overline{K}}{\chi}(\beta\hat{\boldsymbol{n}}\otimes\mathbf{1} + b\mathbf{1}\otimes\hat{\boldsymbol{n}}), \tag{27}$$

where $\chi = 3(\overline{\mu} + \beta b\overline{K})$, $\overline{K} = \overline{\lambda} + (2/3)\overline{\mu}$. The corresponding elastic–plastic acoustic tensor is

$$\boldsymbol{A} = \boldsymbol{n}\cdot\boldsymbol{C}^{\mathrm{ep}}\cdot\boldsymbol{n} = \left(\overline{K} + \frac{\overline{\mu}}{3} - \frac{3\beta b\overline{K}^2}{\chi}\right)\boldsymbol{n}\otimes\boldsymbol{n} + \overline{\mu}\mathbf{1} - \frac{6\overline{\mu}^2}{\chi}\boldsymbol{N}\otimes\boldsymbol{N} - \frac{3\sqrt{2}\overline{\mu}\overline{K}}{\chi}(\beta\boldsymbol{N}\otimes\boldsymbol{n} + b\boldsymbol{n}\otimes\boldsymbol{N}), \tag{28}$$

where $\boldsymbol{N} = \hat{\boldsymbol{n}}\cdot\boldsymbol{n} = \boldsymbol{n}\cdot\hat{\boldsymbol{n}}$. Note that neither $\boldsymbol{C}^{\mathrm{ep}}$ nor $\boldsymbol{A}$ has major symmetry unless $\beta = b$.

The localization condition and slip line orientation are formulated in closed form for plane strain. In the principal stress space, σ_2 is the minor principal stress (major compressive principal stress), σ_1 is the major principal stress, and σ_3 is the intermediate principal stress, such that $0 \geqslant \sigma_1 \geqslant \sigma_3 \geqslant \sigma_2$ and $|\sigma_1| \leqslant |\sigma_3| \leqslant |\sigma_2|$. Refer to Fig. 2 to construct the unit vectors $\boldsymbol{n}$, $\boldsymbol{t}$, and $\boldsymbol{m}$ as

$$\boldsymbol{n} = \begin{Bmatrix} \cos\theta \\ \sin\theta \\ 0 \end{Bmatrix}, \qquad \boldsymbol{t} = \begin{Bmatrix} \sin\theta \\ -\cos\theta \\ 0 \end{Bmatrix}, \qquad \boldsymbol{m} = \begin{Bmatrix} \cos\eta \\ -\sin\eta \\ 0 \end{Bmatrix} = \cos\psi\boldsymbol{t} + \sin\psi\boldsymbol{n}, \tag{29}$$

where $\eta = 90^\circ - \theta - \psi$, and ψ is the jump dilation angle between $\boldsymbol{m}$ and $\boldsymbol{t}$.

Using an eigenvalue analysis similar to that presented in Runesson et al. (1991) – where their acoustic tensor $\boldsymbol{A}$ was determined by a weak discontinuity formulation as opposed to the strong discontinuity formulation presented in this paper – Borja and Regueiro (2001) presented a localization condition as

$$\frac{3\sqrt{2}s_3}{\|\boldsymbol{s}\|} = \sqrt{\frac{2}{1-\nu}}(\beta - b) - (\beta + b), \tag{30}$$

and an equation for the slip line orientation as

$$\theta = \pm\tan^{-1}\left[\sqrt{-\frac{3(s_2 + \nu s_3) + (1+\nu)(\beta+b)\frac{\|\boldsymbol{s}\|}{\sqrt{2}}}{3(s_1 + \nu s_3) + (1+\nu)(\beta+b)\frac{\|\boldsymbol{s}\|}{\sqrt{2}}}}\right], \tag{31}$$

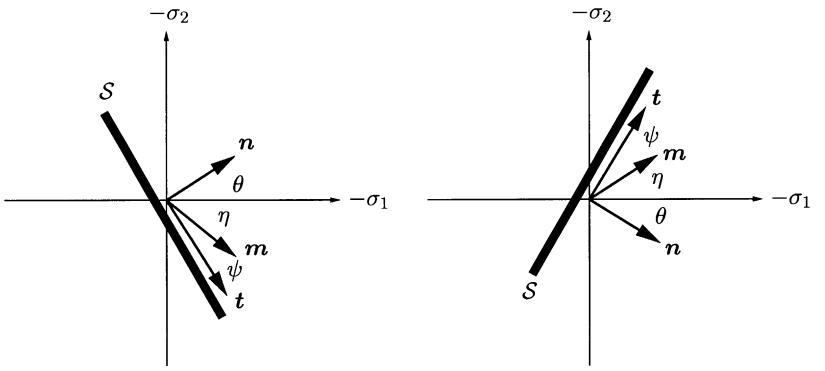

Fig. 2. Slip line orientation with respect to major principal stress axis for $\pm\theta$.

where the denominator in Eq. (31) is less than zero, the numerator is greater than zero, $s_1 = \sigma_1 - p$, etc. Eq. (31) determines the orientation of the normal $\boldsymbol{n}$ to the slip surface $\mathscr{S}$ with respect to the major principal stress axis (Fig. 2). After substituting for $\boldsymbol{n}$ into $\boldsymbol{A}$, the direction $\boldsymbol{m}$ then follows from $\boldsymbol{A} \cdot \boldsymbol{m} = \boldsymbol{0}$, $\det \boldsymbol{A} = 0$, and Eq. (29) as

$$\eta = \tan^{-1}\left(\frac{A_{11}}{A_{12}}\right) = \tan^{-1}\left(\frac{A_{21}}{A_{22}}\right), \tag{32}$$

where for the plane strain case

$$\boldsymbol{A} = \begin{bmatrix} A_{11} & A_{12} & 0 \\ A_{21} & A_{22} & 0 \\ 0 & 0 & \overline{\mu} \end{bmatrix}, \tag{33}$$

and the acoustic tensor components $A_{11}, A_{12}, A_{21}, A_{22}$ are calculated from Eq. (28).

A nonlinear optimization algorithm (e.g., Ortiz et al., 1987) will detect onset of localization at the same stress state as determined by Eq. (30) and with the same slip line orientation as found in Eq. (31).

4.5. Stress–displacement relation for Drucker–Prager plasticity

The stress–displacement relation is the constitutive equation for post-localization plasticity, and in a formulation of plasticity with strong discontinuity, it results from the post-localization consistency condition. Different yield and plastic potential functions can be chosen for the post-localization state (Borja and Regueiro, 2001) because the plasticity solution has bifurcated and because the material body exhibits a different physical (constitutive) response upon undergoing localized deformation. Here, a damage yield function similar to a simple Mohr–Coulomb contact surface failure model (Vermeer and de Borst, 1984; Wan et al., 1990; Borja and Regueiro, 2001) is chosen as

$$f := |(\boldsymbol{n} \otimes \boldsymbol{t})^{\mathrm{s}} : \boldsymbol{\sigma}| - (c - \tan\overline{\phi}(\boldsymbol{n} \otimes \boldsymbol{n} : \boldsymbol{\sigma})) = 0, \tag{34}$$

where $\boldsymbol{t}$ is a unit vector tangent to the discontinuity $\mathscr{S}$, c, a cohesion-like internal state variable on $\mathscr{S}$, and $\overline{\phi}$, the mobilized friction angle on $\mathscr{S}$. A damage plastic potential function is defined similar to Eq. (34) as

$$g := |(\boldsymbol{n} \otimes \boldsymbol{t})^{\mathrm{s}} : \boldsymbol{\sigma}| - (c - \tan\psi(\boldsymbol{n} \otimes \boldsymbol{n} : \boldsymbol{\sigma})), \tag{35}$$

where ψ is the jump dilation angle in Fig. 2. The stress gradient of the damage yield function is

$$\frac{\partial f}{\partial \boldsymbol{\sigma}} = \operatorname{sign}[(\boldsymbol{n} \otimes \boldsymbol{t})^{\mathrm{s}} : \boldsymbol{\sigma}](\boldsymbol{n} \otimes \boldsymbol{t})^{\mathrm{s}} + \tan\overline{\phi}(\boldsymbol{n} \otimes \boldsymbol{n}), \tag{36}$$

and the stress gradient of the damage plastic potential function is

$$\begin{aligned} \frac{\partial g}{\partial \boldsymbol{\sigma}} &= \operatorname{sign}[(\boldsymbol{n} \otimes \boldsymbol{t})^{\mathrm{s}} : \boldsymbol{\sigma}](\boldsymbol{n} \otimes \boldsymbol{t})^{\mathrm{s}} + \tan\psi(\boldsymbol{n} \otimes \boldsymbol{n}) \\ &= \frac{1}{\cos\psi}[\boldsymbol{n} \otimes (\operatorname{sign}[(\boldsymbol{n} \otimes \boldsymbol{t})^{\mathrm{s}} : \boldsymbol{\sigma}]\cos\psi\boldsymbol{t} + \sin\psi\boldsymbol{n})]^{\mathrm{s}} \\ &= \frac{1}{\cos\psi}(\boldsymbol{n} \otimes \boldsymbol{m})^{\mathrm{s}}, \end{aligned} \tag{37}$$

where $\boldsymbol{m}$ is the direction of the jump displacement (Fig. 2) and $\operatorname{sign}[(\boldsymbol{n} \otimes \boldsymbol{t})^{\mathrm{s}} : \boldsymbol{\sigma}]$ determines the direction of $\boldsymbol{t}$. The stress rate must remain regular in the post-localization (damaged) state, at which time Eqs. (9) and (37) lead to

$$\dot{\zeta}(\boldsymbol{m}\otimes\boldsymbol{n})^{\mathrm{s}}=\lambda_{\delta}\frac{\partial g}{\partial\boldsymbol{\sigma}}=\frac{\lambda_{\delta}}{\cos\psi}(\boldsymbol{m}\otimes\boldsymbol{n})^{\mathrm{s}}, \tag{38}$$

which in turn leads to

$$\lambda_{\delta}=\cos\psi\dot{\zeta}. \tag{39}$$

From Eq. (25), it is clear that λ $(=\lambda_{\delta}\delta_{\mathscr{S}})$ represents deviatoric plastic deformation, and subsequently λ_{δ} does as well. Eq. (39) states that λ_{δ} is the tangential component of the jump displacement rate $[\![\dot{\boldsymbol{u}}]\!]$ $(=\dot{\zeta}\boldsymbol{m})$ on $\mathscr{S}$. Note that Eq. (38) is valid because $\partial g/\partial\boldsymbol{\sigma}$ is a rank two tensor.

The consistency condition governing the damaged state becomes

$$\dot{f}=\frac{\partial f}{\partial\boldsymbol{\sigma}}:\dot{\boldsymbol{\sigma}}+\frac{\partial f}{\partial c}\dot{c}=0, \tag{40}$$

where $\dot{\boldsymbol{\sigma}}=\boldsymbol{c}^{\mathrm{e}}:\nabla^{\mathrm{s}}\dot{\overline{\boldsymbol{u}}}$, and $\dot{c}=H_{\delta}\lambda_{\delta}$ (Regueiro and Borja, 1999). Substituting and integrating Eq. (40) leads to the stress–displacement relation as

$$(\boldsymbol{\mu}\otimes\boldsymbol{n})^{\mathrm{s}}:\boldsymbol{\sigma}(t)=(\boldsymbol{\mu}\otimes\boldsymbol{n})^{\mathrm{s}}:\boldsymbol{\sigma}_{\mathrm{loc}}+H_{\delta}\cos\psi\zeta(t), \tag{41}$$

where

$$\boldsymbol{\mu}:=\mathrm{sign}[(\boldsymbol{n}\otimes\boldsymbol{t})^{\mathrm{s}}:\boldsymbol{\sigma}]\boldsymbol{t}+\tan\overline{\phi}\boldsymbol{n}; \tag{42}$$

time $\boldsymbol{t}$ starts at the onset of localization, where $\zeta(0)=0$ and $\boldsymbol{\sigma}(0)=\boldsymbol{\sigma}_{\mathrm{loc}}$, and H_{δ} is the constant localized softening modulus. Note that because H_{δ} is the softening modulus in the post-localization (bifurcated) state, it is unrelated to H. Since it is of interest to model loss of material body strength, $H_{\delta}<0$. Writing Eq. (41) in different form results in

$$Q:=|q_{\mathrm{t}}(t)|+\tan\overline{\phi}(q_{\mathrm{n}}(t)+p(t))-\left[|q_{\mathrm{t,loc}}|+\tan\overline{\phi}(q_{\mathrm{n,loc}}+p_{\mathrm{loc}})+H_{\delta}\cos\psi\zeta(t)\right]=0, \tag{43}$$

where q_{t} and q_{n} are the tangential and normal components, respectively, of the deviatoric traction $\boldsymbol{s}\cdot\boldsymbol{n}$ on discontinuity $\mathscr{S}$, and p is the pressure:

$$\begin{aligned}q_{\mathrm{t}}&=(\boldsymbol{n}\otimes\boldsymbol{t})^{\mathrm{s}}:\boldsymbol{s},\\ q_{\mathrm{n}}&=(\boldsymbol{n}\otimes\boldsymbol{n}):\boldsymbol{s},\\ p&=\mathrm{tr}(\boldsymbol{\sigma})/3.\end{aligned} \tag{44}$$

5. Finite element implementation

The assumed enhanced strain (AES) method (Simo and Rifai, 1990) is the variational framework used in this paper to implement the strong discontinuity approach, and it satisfies the two conditions necessary and sufficient for convergence when an enhanced strain field is introduced: (1) stability, and (2) consistency (i.e., the patch test). In this implementation, the unregularized formulation is used, where the Dirac-delta function is treated directly and not regularized (Armero and Garikipati, 1995; Regueiro and Borja, 1999; Borja and Regueiro, 2001). The discretized variational equations are discussed first, followed by the matrix finite element equations and linearization for solution by the Newton–Raphson method as well as a discussion of the numerical implementation of the localization condition.

5.1. Petrov–Galerkin form

Let $\overline{\Omega}^h$ be the discretization of a closed region $\overline{\Omega}$, and $\overline{\Omega}^h_{\rm loc}$ be the discretization of the localized region $\overline{\Omega}_{\rm loc}$, where $\mathscr{S}^h \subset \overline{\Omega}^h_{\rm loc}$, $\overline{\Omega}^h_{\rm loc} \subset \overline{\Omega}^h$, and h is the discretization parameter. The resulting Petrov–Galerkin form is as follows (Simo and Oliver, 1994; Armero and Garikipati, 1995):

$$\int_{\Omega^h} \nabla^{\rm s}\overline{\boldsymbol{\eta}}^h : \boldsymbol{\sigma}^h {\rm d}\Omega = \int_{\Omega^h} \overline{\boldsymbol{\eta}}^h \cdot \boldsymbol{b}^h {\rm d}\Omega + \int_{\Gamma^h_t} \overline{\boldsymbol{\eta}}^h \cdot \boldsymbol{t}^{\sigma,h} {\rm d}\Gamma, \tag{45a}$$

$$\int_{\Omega^h_{\rm loc}} \tilde{\boldsymbol{\gamma}}^h : \boldsymbol{\sigma}^h {\rm d}\Omega = 0, \tag{45b}$$

where $\overline{\boldsymbol{\eta}}^h = \delta\overline{\boldsymbol{u}}^h$ and $\tilde{\boldsymbol{\gamma}}^h = \delta\tilde{\boldsymbol{\epsilon}}^h$. The symmetric gradient of the continuous part of the displacement variation, $\nabla^{\rm s}\overline{\boldsymbol{\eta}}^h$, belongs to the space

$$\mathscr{E}^h := \left\{\nabla^{\rm s}\overline{\boldsymbol{\eta}}^h : \Omega^h \to \mathbb{S} | \nabla^{\rm s}\overline{\boldsymbol{\eta}}^h \in L_2\right\}, \tag{46}$$

while the enhanced strain variation $\tilde{\boldsymbol{\gamma}}^h$ belongs to the space

$$\tilde{\mathscr{E}}^h := \left\{\tilde{\boldsymbol{\gamma}}^h : \Omega^h_{\rm loc} \to \mathbb{S} | \tilde{\boldsymbol{\gamma}}^h \in L_2\right\}, \tag{47}$$

where L_2 is the zeroth Sobolev space and $\mathscr{E}^h \cap \tilde{\mathscr{E}}^h = \emptyset$ ensures stability of the AES method (Simo and Rifai, 1990). With the reparameterized displacement field (Simo et al., 1993)

$$\boldsymbol{u}^h(\boldsymbol{x},t) = \overline{\boldsymbol{u}}^h(\boldsymbol{x},t) + [\![\boldsymbol{u}^h(t)]\!] M^h_{\mathscr{S}}(\boldsymbol{x}), \qquad M^h_{\mathscr{S}}(\boldsymbol{x}) := H_{\mathscr{S}}(\boldsymbol{x}) - f^h(\boldsymbol{x}), \tag{48}$$

where f^h is the finite element enhancement function, the discretized displacement variation is

$$\boldsymbol{\eta}^h = \delta\boldsymbol{u}^h = \overline{\boldsymbol{\eta}}^h + [\![\boldsymbol{\eta}^h]\!] M^h_{\mathscr{S}}, \qquad [\![\boldsymbol{\eta}^h]\!] = \eta^h \boldsymbol{m}. \tag{49}$$

Thus, the strain $\boldsymbol{\epsilon}^h$ and strain variation $\boldsymbol{\gamma}^h$ become

$$\boldsymbol{\epsilon}^h := \nabla^{\rm s}\boldsymbol{u}^h = \nabla^{\rm s}\overline{\boldsymbol{u}}^h + \tilde{\boldsymbol{\epsilon}}^h, \tag{50}$$

where

$$\tilde{\boldsymbol{\epsilon}}^h = -\zeta^h\left(\boldsymbol{m} \otimes \nabla f^h\right)^{\rm s} + \zeta^h(\boldsymbol{m} \otimes \boldsymbol{n})^{\rm s}\delta_{\mathscr{S}}, \tag{51}$$

and

$$\boldsymbol{\gamma}^h := \nabla^{\rm s}\boldsymbol{\eta}^h = \nabla^{\rm s}\overline{\boldsymbol{\eta}}^h + \tilde{\boldsymbol{\gamma}}^h. \tag{52}$$

The enhanced strain variation $\tilde{\boldsymbol{\gamma}}^h$ is chosen such that Eq. (45b) is satisfied for piecewise constant stress fields (i.e., the patch test is passed, Taylor et al., 1986) such that

$$\int_{\Omega^h_{\rm loc}} \tilde{\boldsymbol{\gamma}}^h {\rm d}\Omega = \boldsymbol{0}. \tag{53}$$

Considering Eq. (53), $\tilde{\boldsymbol{\gamma}}^h$ is chosen to have the following form (Armero and Garikipati, 1995)

$$\tilde{\boldsymbol{\gamma}}^h = \eta^h\left(\delta_{\mathscr{S}^h} - \frac{l_{\mathscr{S}^h}}{A^h}\right)\boldsymbol{F}^h, \tag{54}$$

where $l_{\mathscr{S}^h}$ is the slip line length within $\Omega^h_{\rm loc}$, A^h is the area, and $\boldsymbol{F}^h \in \mathbb{S}$. Thus, via Eq. (54), satisfaction of the patch test is ensured. Because of the enhanced strain variational nature of the AES method, $\tilde{\boldsymbol{\gamma}}^h$ may be chosen arbitrarily. The choice for $\boldsymbol{F}^h$ made in Armero and Garikipati (1995) was $\boldsymbol{F}^h = (\boldsymbol{m} \otimes \boldsymbol{n})^{\rm s}$ which via Eq. (45b) leads to a weak satisfaction of traction equilibrium across the discontinuity $\mathscr{S}^h$. The choice for $\boldsymbol{F}^h$,

however, should in general depend on the constitutive relations governing the post-localization state since the enhanced strain represents the localized deformation. Thus, the appropriate choice for $\boldsymbol{F}^h$ given in Eq. (41) is (Borja and Regueiro, 2001)

$$\boldsymbol{F}^h := \frac{\partial f}{\partial \boldsymbol{\sigma}^h} = \operatorname{sign}[(\boldsymbol{n}\otimes\boldsymbol{t})^{\mathrm{s}} : \boldsymbol{\sigma}^h](\boldsymbol{n}\otimes\boldsymbol{t})^{\mathrm{s}} + \tan\overline{\phi}(\boldsymbol{n}\otimes\boldsymbol{n}), \tag{55}$$

which when substituted into Eqs. (54) and (45b) and using Eq. (43) results in a weak form of Eq. (41) as

$$|q_{\mathscr{S},\mathrm{t}}| + \tan\overline{\phi}(q_{\mathscr{S},\mathrm{n}} + p_{\mathscr{S}}) - \left[|q_{\mathscr{S},\mathrm{t,loc}}| + \tan\overline{\phi}(q_{\mathscr{S},\mathrm{n,loc}} + p_{\mathscr{S},\mathrm{loc}}) + H_\delta \cos\psi\dot{\zeta}^h\right] = 0, \tag{56}$$

where

$$\begin{aligned}
|q_{\mathscr{S},\mathrm{t}}| &:= \frac{1}{l_{\mathscr{S}^h}}\int_{\mathscr{S}^h}|q_{\mathrm{t}}|\mathrm{d}\Gamma = \frac{1}{A^h}\left|\int_{\Omega^h_{\mathrm{loc}}}(\boldsymbol{n}\otimes\boldsymbol{t})^{\mathrm{s}} : \boldsymbol{s}^h\mathrm{d}\Omega\right|,\\
q_{\mathscr{S},\mathrm{n}} &:= \frac{1}{l_{\mathscr{S}^h}}\int_{\mathscr{S}^h}q_{\mathrm{n}}\mathrm{d}\Gamma = \frac{1}{A^h}\int_{\Omega^h_{\mathrm{loc}}}(\boldsymbol{n}\otimes\boldsymbol{n}) : \boldsymbol{s}^h\mathrm{d}\Omega,\\
p_{\mathscr{S}} &:= \frac{1}{l_{\mathscr{S}^h}}\int_{\mathscr{S}^h}p^h\mathrm{d}\Gamma = \frac{1}{A^h}\int_{\Omega^h_{\mathrm{loc}}}p^h\mathrm{d}\Omega.
\end{aligned} \tag{57}$$

Note that the absolute value operator $|\bullet|$ in Eq. (57) was moved outside the integral $\int_{\Omega^h_{\mathrm{loc}}}(\boldsymbol{n}\otimes\boldsymbol{t})^{\mathrm{s}} : \boldsymbol{s}^h\mathrm{d}\Omega$ because since $[\![\boldsymbol{u}(t)]\!]$ in Eq. (5) is spatially invariant, the stress–displacement relation in Eq. (41) governs the *average* stress–displacement response in the localized region Ω^h_{loc} (eventually within a localized element region $\Omega^h_{\mathrm{loc},e}$).

If a uniform strain element is used like the constant strain triangle or the hexahedral element of Belytschko and Bindeman (1993), the AES method can be abandoned for the standard Bubnov–Galerkin method via an implicit treatment of the consistency condition within the stress update (Borja, 2000). This implicit treatment is possible because the jump displacement is assumed spatially invariant in Eq. (5), which leads to a uniform enhanced strain within the localized element.

5.2. Finite element matrix equations

Let $\overline{\Omega}^h = \cup_{e=1}^{n_{\mathrm{el}}}\overline{\Omega}^h_e$ be the finite element discretization of a closed region $\overline{\Omega}$, and $\overline{\Omega}^h_{\mathrm{loc}} = \cup_{e=1}^{n_{\mathrm{el,loc}}}\overline{\Omega}^h_{\mathrm{loc},e}$ be the finite element discretization of the localized region $\overline{\Omega}_{\mathrm{loc}}$, where n_{el} is the number of elements and $n_{\mathrm{el,loc}}$ is the number of localized elements which is not known a priori. The standard finite element interpolations within an element domain $\overline{\Omega}^h_e$ in isoparametric coordinates $\boldsymbol{\xi}$ are

$$\overline{\boldsymbol{u}}^h_e(\boldsymbol{\xi}) = \sum_{A=1}^{n_{\mathrm{nds}}}N^A(\boldsymbol{\xi})\boldsymbol{d}^A_e, \qquad \overline{\boldsymbol{\eta}}^h_e = \sum_{A=1}^{n_{\mathrm{nds}}}N^A(\boldsymbol{\xi})\boldsymbol{c}^A_e, \tag{58}$$

where n_{nds} is the number of nodes of an element e, $N^A(\boldsymbol{\xi})$ is the shape function at node A, and $\boldsymbol{d}^A_e$ and $\boldsymbol{c}^A_e$ are the displacement vector and displacement variation vector, respectively, at node A. The expressions in Eq. (58) in matrix form are

$$\overline{\boldsymbol{u}}^h_e(\boldsymbol{\xi}) = \boldsymbol{N}_e(\boldsymbol{\xi})\cdot\boldsymbol{d}_e, \qquad \overline{\boldsymbol{\eta}}^h_e = \boldsymbol{N}_e(\boldsymbol{\xi})\cdot\boldsymbol{c}_e, \tag{59}$$

where $\boldsymbol{N}_e(\boldsymbol{\xi})$ is the element shape function matrix, and $\boldsymbol{d}_e$ and $\boldsymbol{c}_e$ are the displacement vector and displacement variation vector, respectively, for element e. Taking the symmetric gradient of the expressions in Eq. (59) results in

$$\boldsymbol{\nabla}^{\mathrm{s}}\overline{\boldsymbol{u}}^h_e(\boldsymbol{\xi}) = \boldsymbol{B}_e(\boldsymbol{\xi})\cdot\boldsymbol{d}_e, \qquad \boldsymbol{\nabla}^{\mathrm{s}}\overline{\boldsymbol{\eta}}^h_e = \boldsymbol{B}_e(\boldsymbol{\xi})\cdot\boldsymbol{c}_e, \tag{60}$$

where $\boldsymbol{B}_e(\boldsymbol{\xi})$ is the element strain–displacement matrix. Likewise, from Eqs. (51), (52), (54), and (55), $\tilde{\boldsymbol{\epsilon}}^h$ and $\tilde{\boldsymbol{\gamma}}^h$ in matrix form for a localized element domain $\overline{\Omega}^h_{\mathrm{loc},e}$ are

$$\tilde{\boldsymbol{\epsilon}}^h_e = -\boldsymbol{G}_e\zeta^h_e + \boldsymbol{F}_e\zeta^h_e\delta_{\mathscr{S}_e}, \qquad \boldsymbol{G}_e = \left[(\boldsymbol{m}_e \otimes \boldsymbol{\nabla} f^h_e)^{\mathrm{s}}\right], \tag{61}$$

and

$$\tilde{\boldsymbol{\gamma}}^h_e = \eta^h_e\left(\delta_{\mathscr{S}_e} - \frac{l_{\mathscr{S}_e}}{A_e}\right)\boldsymbol{F}_e, \qquad \boldsymbol{F}_e = [(\boldsymbol{\mu}_e \otimes \boldsymbol{n}_e)^{\mathrm{s}}], \tag{62}$$

where

$$\boldsymbol{\mu}_e := \mathrm{sign}\left(\int_{\Omega^h_{\mathrm{loc},e}} (\boldsymbol{n}_e \otimes \boldsymbol{t}_e)^{\mathrm{s}} : \boldsymbol{\sigma}^h \mathrm{d}\Omega\right)\boldsymbol{t}_e + \tan\overline{\phi}\boldsymbol{n}_e, \tag{63}$$

where $[\bullet]$ denotes matrix form of a tensor. Substituting the matrix expressions for $\overline{\boldsymbol{\eta}}^h_e$ from Eqs. (59), $\boldsymbol{\nabla}^{\mathrm{s}}\overline{\boldsymbol{\eta}}^h_e$ from Eq. (60), and $\tilde{\boldsymbol{\gamma}}^h_e$ from Eq. (62) into Eqs. (45a) and (45b), and assuming arbitrary values of $\boldsymbol{c}_e$ and η^h_e, the nonlinear finite element equations expressed in residual form result as

$$\begin{aligned} \boldsymbol{R}_e &:= \int_{\Omega^h_e} \boldsymbol{B}^{\mathrm{T}}_e\boldsymbol{\sigma}^h \mathrm{d}\Omega - \int_{\Omega^h_e} \boldsymbol{N}^{\mathrm{T}}_e\boldsymbol{b}^h \mathrm{d}\Omega - \int_{\Gamma^h_{\mathrm{t},e}} \boldsymbol{N}^{\mathrm{T}}_e\boldsymbol{t}^{\sigma,h} \mathrm{d}\Gamma = \boldsymbol{0}, \\ r_e &:= |q_{\mathscr{S}_e,\mathrm{t}}| + \tan\overline{\phi}(q_{\mathscr{S}_e,\mathrm{n}} + p_{\mathscr{S}_e}) - \left[|q_{\mathscr{S}_e,\mathrm{t,loc}}| + \tan\overline{\phi}(q_{\mathscr{S}_e,\mathrm{n,loc}} + p_{\mathscr{S}_e,\mathrm{loc}}) + H_\delta\cos\psi\zeta_e\right] = 0, \end{aligned} \tag{64}$$

where $\boldsymbol{R}_e$ is the standard residual for balance of linear momentum associated with the nodal degrees of freedom for an element e, r_e is the residual expressing the weak form of Eq. (41) on the discontinuity $\mathscr{S}_e$ associated with the jump displacement degree of freedom within element e, and $\boldsymbol{\sigma}^h$ is in vector form.

With the reparameterization of the displacement field in Eq. (48), the stress rate becomes

$$\dot{\boldsymbol{\sigma}}^h = \boldsymbol{D}^{\mathrm{e}} \cdot \left[\dot{\tilde{\boldsymbol{\epsilon}}}^h_e - \boldsymbol{G}_e\dot{\zeta}^h_e\right] \quad \text{in} \quad \Omega^h_{\mathrm{loc},e}/\mathscr{S}_e, \tag{65}$$

where $\boldsymbol{D}^{\mathrm{e}}$ is the matrix form of $\boldsymbol{c}^{\mathrm{e}}$ in Eq. (16) and $\dot{\tilde{\boldsymbol{\epsilon}}}^h_e = \boldsymbol{\nabla}^{\mathrm{s}}\dot{\tilde{\boldsymbol{u}}}^h_e$. For subsequent derivations, the discretization flag h is left off certain terms. Integrating Eq. (65) results in

$$\boldsymbol{\sigma}^{k+1}_{n+1} = \boldsymbol{\sigma}^{\mathrm{tr}}_{n+1} - \boldsymbol{D}^{\mathrm{e}} \cdot \boldsymbol{G}_e\Delta\zeta_e \quad \text{in} \quad \Omega^h_{\mathrm{loc},e}/\mathscr{S}_e, \tag{66}$$

where $\boldsymbol{\sigma}^{\mathrm{tr}}_{n+1} = \boldsymbol{\sigma}_{\mathrm{n}} + \boldsymbol{D}^{\mathrm{e}} \cdot \Delta\overline{\boldsymbol{\epsilon}}_e$ is the trial stress, $\Delta\overline{\boldsymbol{\epsilon}}_e = \overline{\boldsymbol{\epsilon}}^{k+1}_{e,n+1} - \overline{\boldsymbol{\epsilon}}_{e,\mathrm{n}}$, $\Delta\zeta_e = \zeta^{k+1}_{e,n+1} - \zeta_{e,\mathrm{n}}$, $n+1$ is the current time step, and $k+1$ is the current iteration of a nonlinear solution algorithm. Thus, the term subtracted from the right-hand side of Eq. (66) may be thought of as a correction to the trial stress because the enhancement is already contained within the localized element whose nodal displacements are the total displacements. The algorithmic form of the stress displacement relation (43) is

$$\begin{aligned} |q^{k+1}_{\mathscr{S}_e,\mathrm{t},n+1}| + \tan\overline{\phi}(q^{k+1}_{\mathscr{S}_e,\mathrm{n},n+1} + p^{k+1}_{\mathscr{S}_e,n+1}) = |q_{\mathscr{S}_e,\mathrm{t,loc}}| + \tan\overline{\phi}(q_{\mathscr{S}_e,\mathrm{n,loc}} + p_{\mathscr{S}_e,\mathrm{loc}}) + H_\delta \\ \times \cos\psi|\zeta^{k+1}_{e,n+1}| \quad \text{on} \quad \mathscr{S}_e. \end{aligned} \tag{67}$$

Note that if the sign convention changes from continuum mechanics convention ($\epsilon > 0$ and $\sigma > 0$ in tension for one dimension) to soil mechanics convention ($\epsilon > 0$ and $\sigma > 0$ in compression), Eq. (67) would still be valid if an appropriate sign change was made before the pressure terms in the damage yield and plastic potential functions in Eqs. (34) and (35).

For post-localization, to determine plastic loading and unloading along $\mathscr{S}_e$, the weak form of the trial residual stress needs to be calculated:

$$Q^{\mathrm{tr}}_{n+1} = |q^{\mathrm{tr}}_{\mathscr{S}_e,\mathrm{t},n+1}| + \tan\overline{\phi}(q^{\mathrm{tr}}_{\mathscr{S}_e,\mathrm{n},n+1} + p^{\mathrm{tr}}_{\mathscr{S}_e,n+1}) - \left[|q_{\mathscr{S}_e,\mathrm{t,loc}}| + \tan\overline{\phi}(q_{\mathscr{S}_e,\mathrm{n,loc}} + p_{\mathscr{S}_e,\mathrm{loc}}) + H_\delta \cos\psi|\zeta_{e,\mathrm{n}}|\right], \tag{68}$$

where

$$\begin{aligned}
&\texttt{if}\quad Q^{\mathrm{tr}}_{n+1} > 0 \quad \texttt{then}\quad \text{jump displacement } \zeta^{k+1}_{e,n+1} \text{ evolves on } \mathscr{S}_e \text{ via (66) and (67)}\\
&\texttt{else}\quad q_{\mathscr{S}_e,\mathrm{t},n+1} = q^{\mathrm{tr}}_{\mathscr{S}_e,\mathrm{t},n+1}; \qquad q_{\mathscr{S}_e,\mathrm{n},n+1} = q^{\mathrm{tr}}_{\mathscr{S}_e,\mathrm{n},n+1};\\
&\qquad p_{\mathscr{S}_e,n+1} = p^{\mathrm{tr}}_{\mathscr{S}_e,n+1}; \qquad \zeta_{e,n+1} = \zeta_{e,\mathrm{n}}; \qquad \boldsymbol{\sigma}_{n+1} = \boldsymbol{\sigma}^{\mathrm{tr}}_{n+1};\\
&\texttt{endif}
\end{aligned} \tag{69}$$

The tangential component of traction $q_{\mathscr{S}_e,\mathrm{t}}$ on $\mathscr{S}_e$ must not soften less than a prescribed residual value $q_{\mathscr{S}_e,t,\mathrm{resid}}$, and the normal component of deviatoric traction $q_{\mathscr{S}_e,\mathrm{n}}$ plus the pressure $p_{\mathscr{S}_e}$ must not be in tension (i.e., a tension cut-off for Eq. (34)). Thus, the following checks are made:

$$\begin{aligned}
&\texttt{if}\quad |q^{k+1}_{\mathscr{S}_e,\mathrm{t},n+1}| < q_{\mathscr{S}_e,\mathrm{t,resid}} \quad \texttt{then}\quad q^{k+1}_{\mathscr{S}_e,\mathrm{t},n+1} = q_{\mathscr{S}_e,\mathrm{t,resid}}; \qquad H_\delta = 0;\\
&\qquad \boldsymbol{\mu}_e = \tan\overline{\phi}\boldsymbol{n}_e;\\
&\texttt{if}\quad (q^{k+1}_{\mathscr{S}_e,\mathrm{n},n+1} + p^{k+1}_{\mathscr{S}_e,n+1}) > 0 \quad \texttt{then}\quad (q^{k+1}_{\mathscr{S}_e,\mathrm{n},n+1} + p^{k+1}_{\mathscr{S}_e,n+1}) = 0;\\
&\qquad \boldsymbol{\mu}_e = \mathrm{sign}\left(\int_{\Omega^h_{\mathrm{loc},e}} (\boldsymbol{n}_e \otimes \boldsymbol{t}_e)^{\mathrm{s}} : \boldsymbol{\sigma}^h \mathrm{d}\Omega\right)\boldsymbol{t}_e.
\end{aligned} \tag{70}$$

By setting $H_\delta = 0$, the jump displacement along $\mathscr{S}_e$ may continue to evolve but without the resolved stress on $\mathscr{S}_e$ being softened further. Thus, the stress update for a localized element e is fully defined by Eq. (66) through Eq. (70).

Linearization of the nonlinear finite element equations in Eq. (64) for solution by the Newton–Raphson method (refer to Simo and Hughes, 1998) results in

$$\begin{aligned}
-\boldsymbol{R}^k_{e,n+1} &= \boldsymbol{K}_{dd}\cdot\delta\boldsymbol{d}_e + \boldsymbol{K}_{d\zeta}\delta\zeta_e,\\
-r^k_{e,n+1} &= \boldsymbol{K}_{\zeta d}\cdot\delta\boldsymbol{d}_e + K_{\zeta\zeta}\delta\zeta_e,
\end{aligned} \tag{71}$$

where

$$\begin{aligned}
\boldsymbol{K}_{dd} &= \int_{\Omega^h_e} \boldsymbol{B}^{\mathrm{T}}_e \boldsymbol{D}^{\mathrm{e}} \boldsymbol{B}_e \mathrm{d}\Omega,\\
\boldsymbol{K}_{d\zeta} &= -\int_{\Omega^h_e} \boldsymbol{B}^{\mathrm{T}}_e \boldsymbol{D}^{\mathrm{e}} \boldsymbol{G}_e \mathrm{d}\Omega,\\
\boldsymbol{K}_{\zeta d} &= \frac{1}{A_e}\int_{\Omega^h_{e,\mathrm{loc}}} \boldsymbol{F}^{\mathrm{T}}_e \boldsymbol{D}^{\mathrm{e}} \boldsymbol{B}_e \mathrm{d}\Omega,\\
K_{\zeta\zeta} &= -\frac{1}{A_e}\int_{\Omega^h_{e,\mathrm{loc}}} \boldsymbol{F}^{\mathrm{T}}_e \boldsymbol{D}^{\mathrm{e}} \boldsymbol{G}_e \mathrm{d}\Omega - H_\delta \cos\psi \,\mathrm{sign}(\zeta^{k+1}_{e,n+1}),
\end{aligned} \tag{72}$$

and $\delta\boldsymbol{d}_e = \boldsymbol{d}^{k+1}_{n+1} - \boldsymbol{d}^k_{n+1}$, $\delta\zeta_e = \zeta^{k+1}_{n+1} - \zeta^k_{n+1}$. Since strain due to the jump displacement is treated as an enhanced strain (Eq. (51)), the jump displacement ζ_e may be assumed discontinuous between elements and thus may be condensed out of the equations at the element level to form the reduced system

$$-\tilde{\boldsymbol{R}}^k_{e,n+1} = \tilde{\boldsymbol{K}}_{dd}\cdot\delta\boldsymbol{d}_e, \tag{73}$$

where

$$\tilde{\boldsymbol{R}}^k_{e,n+1} = \boldsymbol{R}^k_{e,n+1} - \boldsymbol{K}_{d\zeta} K^{-1}_{\zeta\zeta} r^k_{e,n+1}, \tag{74}$$

$$\tilde{\boldsymbol{K}}_{dd} = \boldsymbol{K}_{dd} - \boldsymbol{K}_{d\zeta} K^{-1}_{\zeta\zeta} \boldsymbol{K}_{\zeta d}. \tag{75}$$

The jump displacement increment $\delta\zeta_e$ is then updated at each iteration via

$$\delta\zeta_e = -K^{-1}_{\zeta\zeta}(r^k_{e,n+1} + \boldsymbol{K}_{\zeta d} \cdot \delta \boldsymbol{d}_e). \tag{76}$$

5.3. Numerical implementation of the localization condition

The numerical implementation of the localization condition in Eq. (30), which is checked at each Gauss point at the end of a converged time step t_{n+1}, is as follows:

$$\texttt{if} \quad \left| \frac{3\sqrt{2} s_{3,n+1}}{\|\mathrm{s}_{n+1}\|} - \left(\sqrt{\frac{2}{1-v}}(\beta - b) - (\beta + b) \right) \right| \leqslant h^{\mathrm{tol}} \quad \texttt{or} \quad \det \mathbf{A}_{n+1} \leqslant 0, \tag{77}$$

$\texttt{then}$ the element has localized,

where $h^{\mathrm{tol}} = 1 \times 10^{-5}$ is chosen. Depending on the time step size, $\det \mathrm{A}_{n+1} \leqslant 0$ may be met rather than the first inequality in Eq. (77), but this first inequality will be met to the finest tolerance h^{tol} so desired if the time step is refined enough. Upon detection of discontinuous displacement fields within finite elements via Eq. (77), the slip surface orientations are determined by Eq. (31). An algorithm was developed which chooses $+\theta$ or $-\theta$ depending on the element deformation at onset of localization (Regueiro, 1998).

6. Numerical examples

Two numerical examples are presented to demonstrate the model's ability to represent localized deformation occurring in pressure sensitive materials in a mesh-independent manner. Enhanced bilinear quadrilateral elements are used with standard 2×2 numerical integration for dilative plastic deformation and $\overline{B}$ (Hughes, 1980) for deviatoric. The scale factor for displacements of deformed meshes is 1.0 unless otherwise noted. An absolute convergence tolerance of 10^{-10} is used for the Euclidean norm of the residual in Eq. (73) for the Newton–Raphson iteration. For this paper, the jump dilation angle ψ is determined from Eqs. (29) and (32) at localization, but ψ could be chosen separately for the post-localization state.

6.1. Plane strain compression of Gosford sandstone

The experimental results of Ord et al. (1991) are analyzed using the model presented in this paper (refer to Regueiro et al. (1998b) for previous analysis). The material constants are shown in Table 1 for confining pressure $\sigma_c = 20$ MPa. The experimental setup is shown in Fig. 3. In Borja and Regueiro (2001), a weak element (slightly lower yield stress) was selected for one case to demonstrate the difference between the uniform stress solution and the nearly uniform one. The difference was negligible. The selection of the location of a weak element is just as arbitrary as choosing where the slip line begins in a mesh with no weak elements. Thus, for this example no weak elements are selected, and the location of the slip line is chosen similar to that observed in the experiment. For the slope example in Section 6.2, a nonuniform stress field naturally results from the boundary value problem, and thus the start of the slip line is determined.

Table 1
Material parameters for plane strain compression of Gosford sandstone

E	15 MPa
v	0.3
$\overline{\alpha}$	13 kPa
β	0.5
b	0.35
$\overline{\phi}$	30.0°
ψ	≈22°
H	−1 MPa
H_δ	–20 MPa/m
$q_{\mathscr{S},\mathrm{t,resid}}$	0.0 kPa

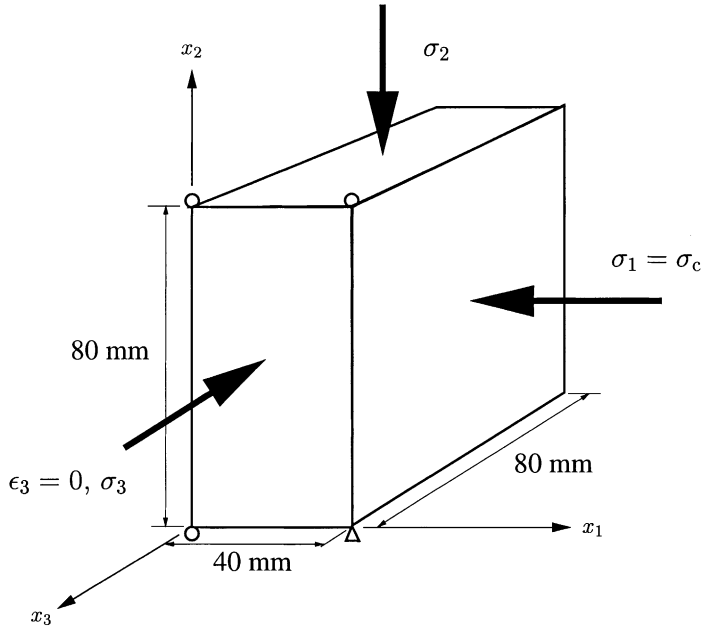

Fig. 3. Finite element model boundary conditions and dimensions for plane strain compression of Gosford sandstone. Confining pressure is $\sigma_c = 20$ MPa. Prescribed displacement of top loading platen results in reaction load P, from which σ_2 may be calculated.

Deformed meshes for the standard and enhanced solutions are shown in Figs. 4 and 5. Note that in Fig. 4, localized deformation is observed even without perturbing the uniform stress state (i.e., by weakening an element, tapering the geometry, or allowing a small amount of friction at the contact platens). This is reflected in the standard solution load–displacement plots in Fig. 6 showing a marked softening behavior upon localized deformation, and the mesh dependence thereof. The x_1 displacement of the node at the upper right corner of the 512 element mesh in Fig. 4 is not fixed. These localized meshes are a result of the ill posed governing PDE which stems from rate-independent strain softening plasticity. Without a material or geometric inhomogeneity, localized deformation could be triggered by LU decomposition of the linear system or the radial return algorithm. For the enhanced solution curves in Fig. 6, the results are clearly mesh independent capturing the same amount of dissipation for each mesh, with the residual stress $q_{\mathscr{S},\mathrm{t,resid}}$ reached at approximately 1.2 mm displacement. In Fig. 6, the reaction load offset at zero displacement is the load due to the confining pressure.

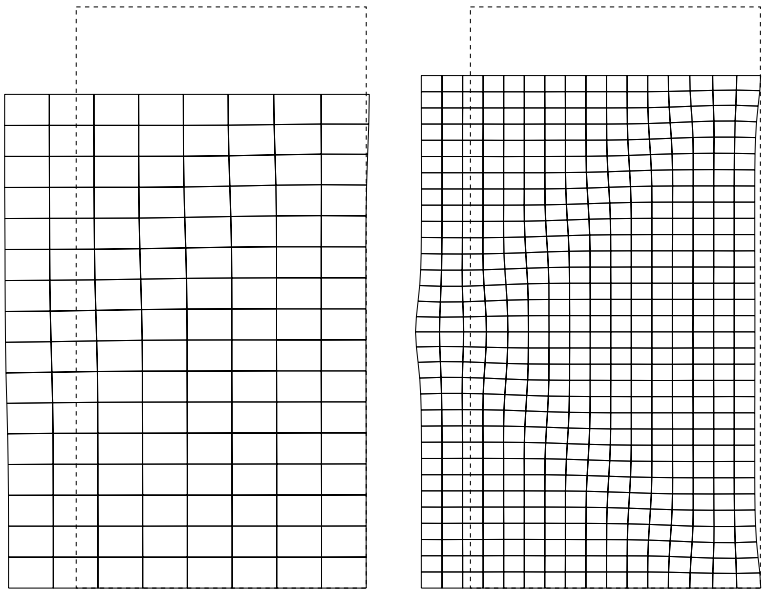

Fig. 4. Deformed meshes for standard solutions with nonassociative, dilative plastic flow: $\beta = 0.5, b = 0.35$, 128 and 512 bilinear quadrilateral elements. Displacements are magnified by a factor of 10.0.

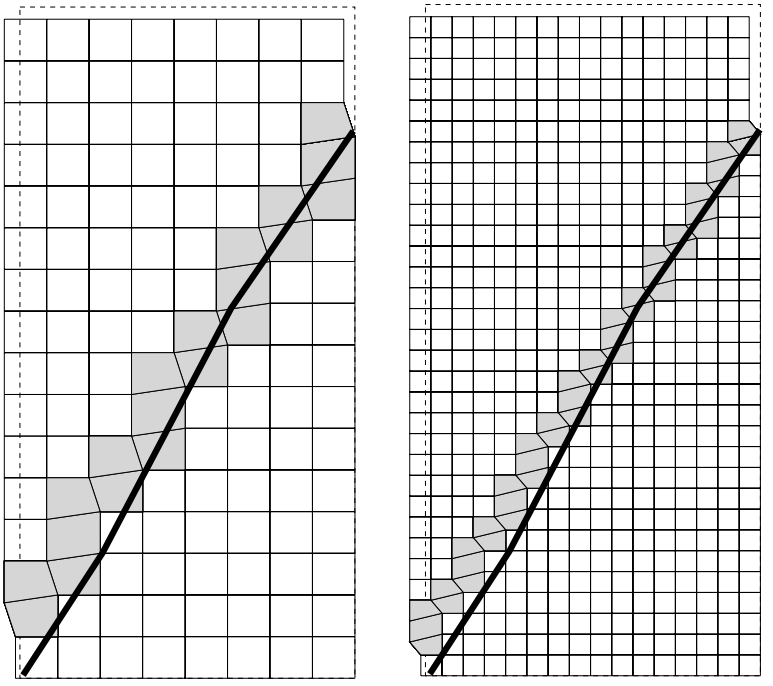

Fig. 5. Deformed meshes for enhanced solutions with nonassociative, dilative plastic flow: $\beta = 0.5, b = 0.35$, 128 and 512 bilinear quadrilateral elements. Localized elements are shaded. Experimental failure surface orientation is drawn as a thick line on each mesh.

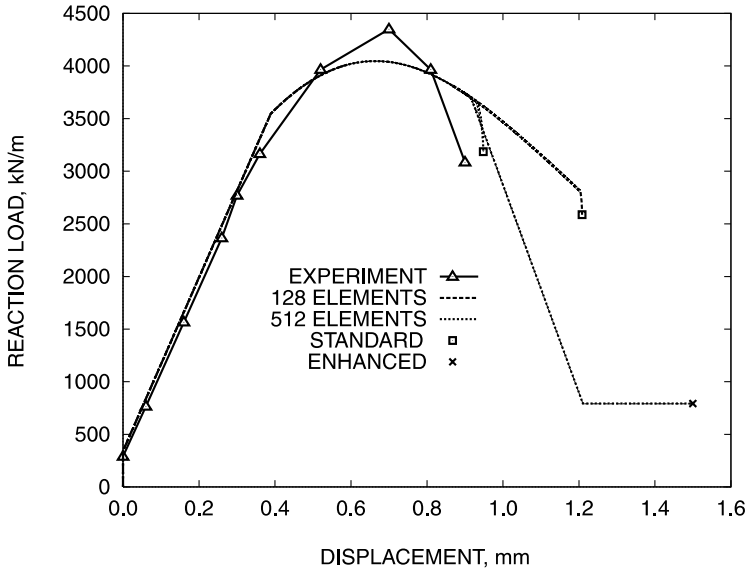

Fig. 6. Load–displacement plots for nonassociative, dilative plastic flow: $\beta = 0.5, b = 0.35$. Enhanced solution curves are the same demonstrating mesh independence. Standard solution curves demonstrate mesh dependence.

6.2. Plane strain slope stability

A slope stability problem is now presented to demonstrate the model's ability to represent localized deformation in a classical geotechnical structure in a nearly mesh-independent manner. Material parameters are shown in Table 2 for nonassociative deviatoric and nonassociative dilative plastic flow: $b = 0.0, 0.05$. If b is chosen any larger, the slip line encounters the base of the mesh, and the numerical solution does not converge further. A gravity load is first applied, the displacements are reset to zero, and a downward displacement is prescribed at the middle of a rigid footing resting at the crest of the slope. The downward displacement may represent the settlement due to a structure placed at the crest of the slope. The dimensions and boundary conditions of the problem are designated in Fig. 7. No weak elements are specified since the boundary value problem inherently generates a nonuniform stress field where, as expected, the element adjacent to the corner of the rigid footing localizes first. This is a fictitious example and not an attempt to model the behavior of an actual soil embankment, although the material parameters are

Table 2
Material parameters for slope stability problem

E	10 MPa
v	0.4
$\overline{\alpha}$	40 kPa
β	0.3
b	0.0, 0.05
$\overline{\phi}$	10.0°
ψ	≈0.9°, ≈3.7°
H	0
H_δ	–100 kPa/m
$q_{\mathscr{S},\mathrm{t,resid}}$	0.0 kPa
γ	20 kN/m^3

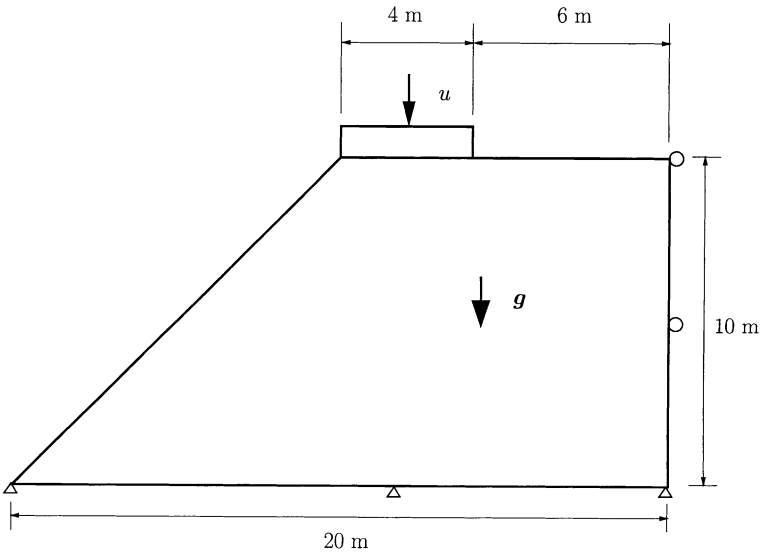

Fig. 7. Slope stability problem. Gravity load $\boldsymbol{g}$ applied before footing displacement u is prescribed.

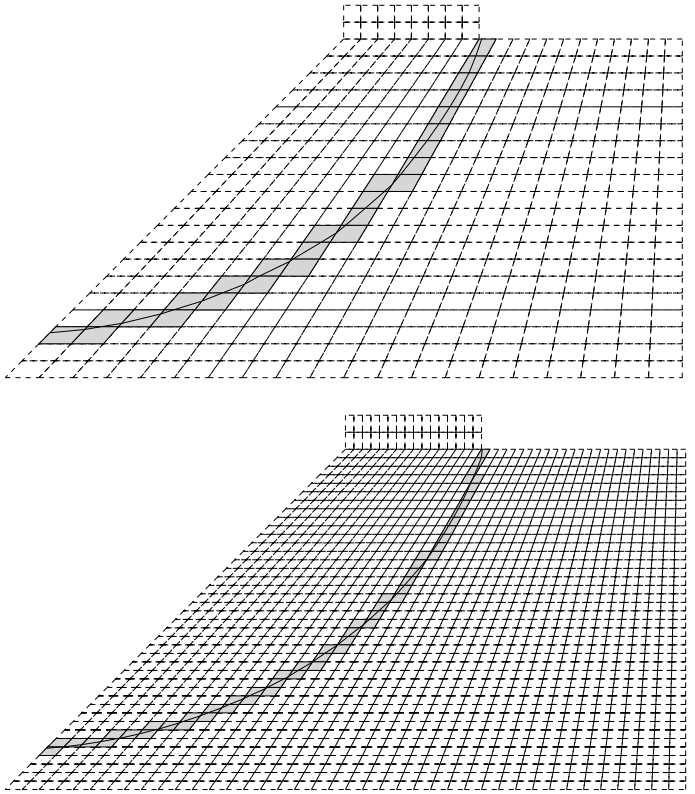

Fig. 8. Undeformed meshes showing slip line orientation for enhanced solutions with nonassociative, deviatoric plastic flow: $\beta = 0.3, b = 0.0$, 400 and 1600 bilinear quadrilateral elements. Slip lines are drawn through localized elements, which are shaded.

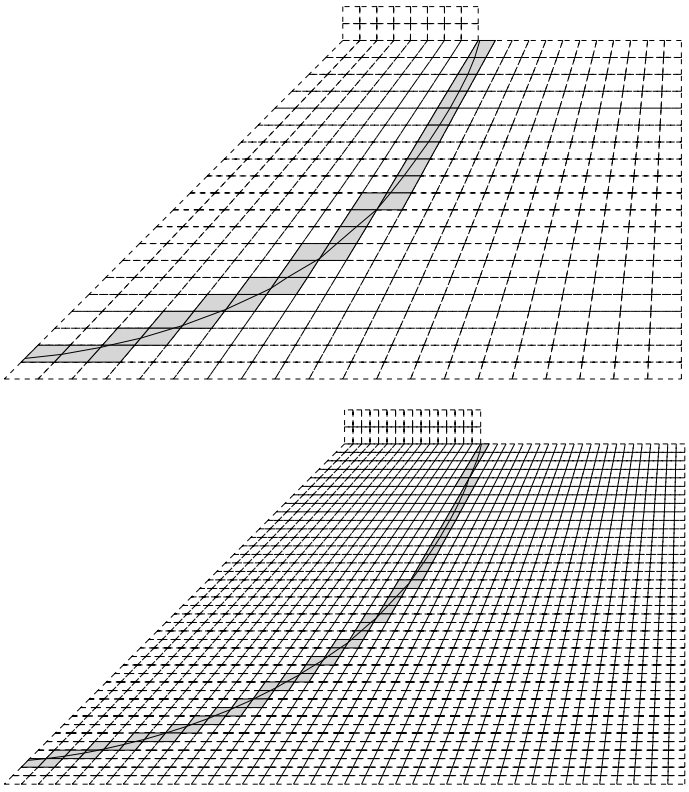

Fig. 9. Undeformed meshes showing slip line orientation for enhanced solutions with nonassociative, dilative plastic flow: $\beta = 0.3, b = 0.05$, 400 and 1600 bilinear quadrilateral elements. Slip lines are drawn through localized elements, which are shaded.

chosen to approximately represent those of a soil. Two meshes with 400 and 1600 bilinear quadrilateral elements are used to analyze the problem.

Figs. 8 and 9 show the slip line orientations on the undeformed meshes for each dilation constant b (0.0, 0.05). Shaded elements are those through which the slip line has traced. Insensitivity to mesh alignment is demonstrated by the slip line tracing across elements without element sides being aligned with the slip line orientation and by slip lines having the same orientation for the 400 and 1600 element meshes. The slip line initiates in the element just to the right of the rigid footing corresponding with the load at which the standard and enhanced solution curves begin to deviate from one another as seen in Figs. 10 and 11. The load at which the enhanced solution curve begins to soften is the load at which the slip line has fully propagated through the mesh. Note the different slip line curvatures in Figs. 8 and 9. The slip line in Fig. 8 has a smaller radius of curvature than the slip line in Fig. 9. This is due to different dilation constants used in each case.

Figs. 12–15 show deformed meshes at end of loading for the standard and enhanced solutions. Note the diffuse deformation patterns for the standard solutions and the sharp localized deformation for the enhanced solutions. Note that in Figs. 13 and 15, for the 1600 element mesh certain localized elements appear to have closed on themselves. This is possible for small strain analyses, but for finite deformation analyses, the simulations would not have been able to proceed as far as they did in Figs. 13 and 15 because finite element volume must remain positive. One way to address this problem is to implement the strong discontinuity plasticity model within the framework of a mesh-free method (Belytschko et al., 1996; Liu et al., 1999), thus abandoning the AES method. Such an implementation is presently being considered. Another

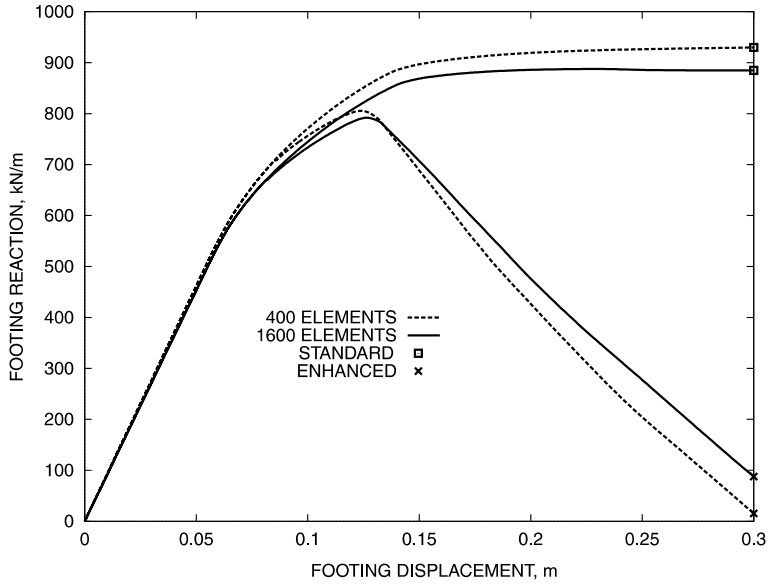

Fig. 10. Load–displacement plots for nonassociative, deviatoric plastic flow: $\beta = 0.3, b = 0.0$. Similar softening slopes of enhanced solution curves demonstrate near objectivity with respect to mesh refinement.

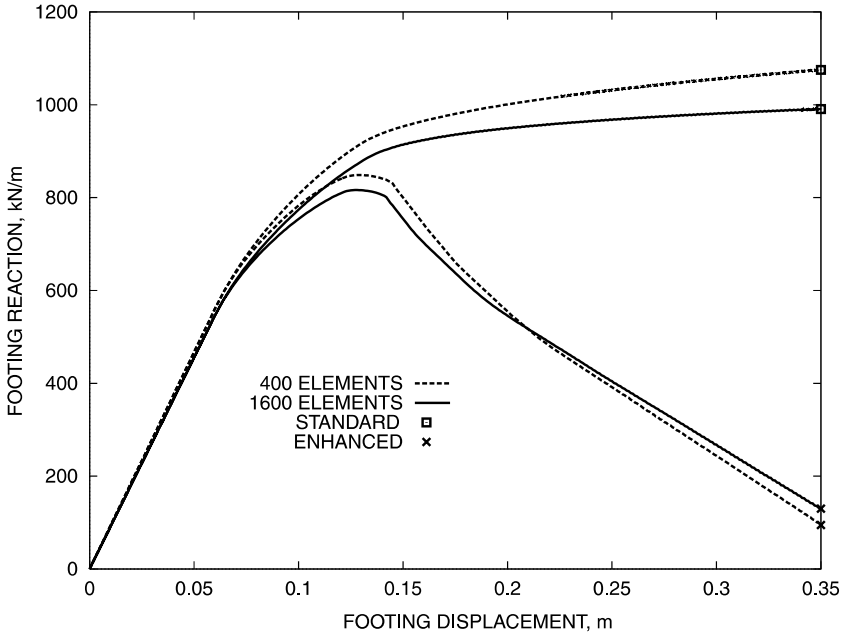

Fig. 11. Load–displacement plots for nonassociative, dilative plastic flow: $\beta = 0.3, b = 0.05$. Similar softening slopes of enhanced solution curves demonstrate near objectivity with respect to mesh refinement.

way would be to remesh in order to introduce a free surface along the slip surface geometry defined by the localization condition in each element.

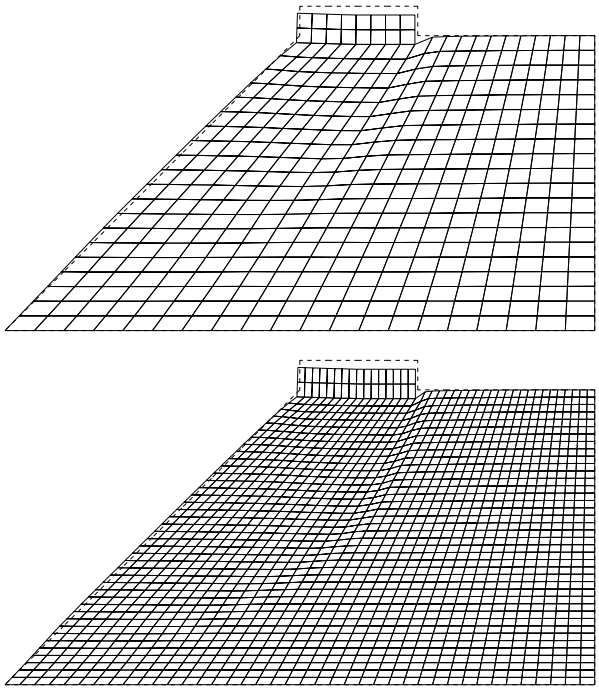

Fig. 12. Deformed meshes for standard solutions with nonassociative, deviatoric plastic flow: $\beta = 0.3, b = 0.0$, 400 and 1600 bilinear quadrilateral elements with $\overline{B}$.

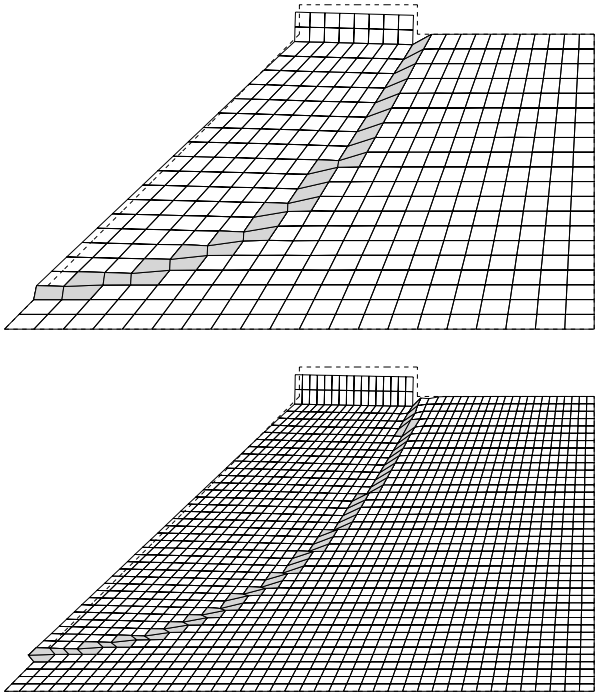

Fig. 13. Deformed meshes for enhanced solutions with nonassociative, deviatoric plastic flow: $\beta = 0.3, b = 0.0$, 400 and 1600 bilinear quadrilateral elements with $\overline{B}$. Localized elements are shaded.

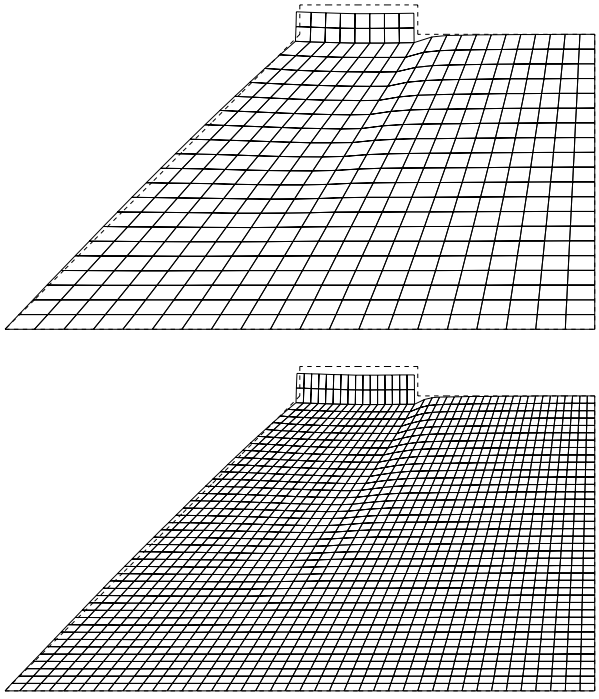

Fig. 14. Deformed meshes for standard solutions with nonassociative, dilative plastic flow: $\beta = 0.3, b = 0.05$, 400 and 1600 bilinear quadrilateral elements.

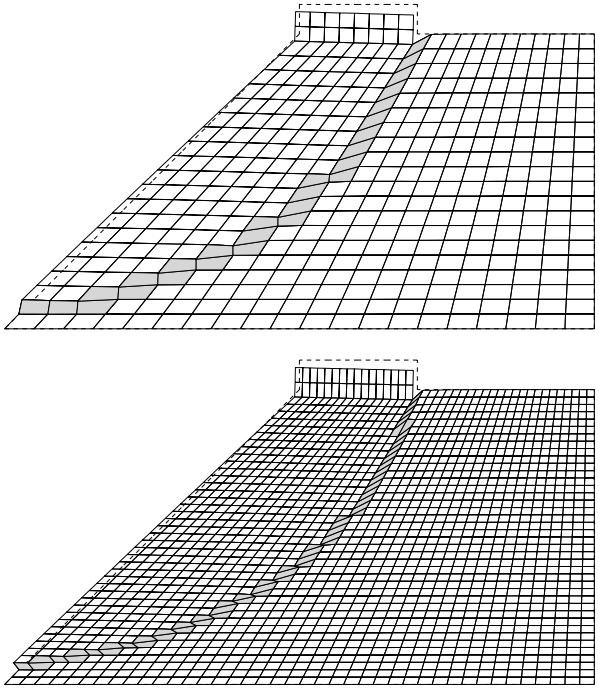

Fig. 15. Deformed meshes for enhanced solutions with nonassociative, dilative plastic flow: $\beta = 0.3, b = 0.05$, 400 and 1600 bilinear quadrilateral elements. Localized elements are shaded.

The similar slopes of the enhanced solution curves in Figs. 10 and 11 demonstrate near mesh independence of the model, where $(q^{k+1}_{\mathscr{S}_e,\mathrm{n},n+1} + p^{k+1}_{\mathscr{S}_e,n+1}) > 0$ is detected for certain localized elements and set $= 0$ via Eq. (70); for the Gosford sandstone example of the previous section, $(q^{k+1}_{\mathscr{S}_e,\mathrm{n},n+1} + p^{k+1}_{\mathscr{S}_e,n+1}) < 0$ in the localized elements and thus stays in compression.

7. Conclusions

A rate-independent, nonassociative, strain-softening Drucker–Prager plasticity model has been formulated in plane strain in the context of strong discontinuities and implemented along with an enhanced bilinear quadrilateral element within the framework of an assumed enhanced strain finite element method. Finite element analyses of localized deformation occurring in a Gosford sandstone parallelepiped and a soil slope have been conducted in a mesh-independent manner (nearly mesh independent for the slope stability problem). The effect of dilatancy on the orientation of slip lines has been demonstrated for the slope stability example.

It is important to simulate the structural phenomenon of localized deformation and the associated loss of material body strength as accurately as possible via a finite element model but to do so in a mesh-independent manner. The strong discontinuity approach is one way to achieve this aim.

The phenomenological model presented in this paper needs to be improved before it can attempt to predict localized deformation in geomaterials. Future work includes extending the model for three-dimensional analysis, incorporating the fluid phase and nonlinear geometric effects, and considering a shear-band-to-slip-surface transition.

Acknowledgements

This work was supported by the G3S Division of the National Science Foundation through Grant no. CMS97-00426 under the direction of Dr. Priscilla P. Nelson and by the Advanced Computational Technology Initiative (ACTI) sponsored by the United States Department of Energy. Mike Stone of Sandia coordinated the ACTI support. This support is gratefully acknowledged. Sandia is a multiprogram laboratory operated by Sandia Corporation, a Lockheed Martin Company, for the United States Department of Energy under contract DE-ACO4-94AL85000.

References

Aifantis, E.C., 1984. On the microstructural origin of certain inelastic models. J. Engng. Mater. Technol. ASME 106, 326–330.

Armero, F., Garikipati, K., 1995. Recent advances in the analysis and numerical simulation of strain localization in inelastic solids. In: Owen, D.R.J., Onate, E., Hinton, E. (Eds.), Proceedings of Computational Plasticity IV, CIMNE. Barcelona, Spain, pp. 547–561.

Armero, F., Garikipati, K., 1996. An analysis of strong discontinuities in multiplicative finite strain plasticity and their relation with the numerical simulation of strain localization in solids. Int. J. Solids Struct. 33, 2863–2885.

Armero, F., 1999. Large-scale modeling of localized dissipative mechanisms in a local continuum: applications to the numerical simulation of strain localization in rate-dependent inelastic models. Mech. Cohesive-Frict. Mater. 4, 101–132.

Aydin, A., Johnson, A.M., 1983. Analysis of faulting in porous sandstone. J. Struct. Geol. 5, 19–31.

Bammann, D.J., 2001. Introduction of a physical length scale into crystal plasticity. J. Eng. Mat. Tech. ASME, submitted for publication.

Bammann, D.J., Mosher, D., Hughes, D.A., Moody, N.R., Dawson, P.R., 1999. Using spatial gradients to model localization phenomena. Sandia National Laboratories Report SAND99-8588.

Belytschko, T., Bindeman, L.P., 1993. Assumed strain stabilization of the eight node hexahedral element. Comput. Meth. Appl. Mech. Engng. 105, 225–260.

Belytschko, T., Krongauz, Y., Organ, D., Fleming, M., Krysl, P., 1996. Meshless methods: an overview and recent developments. Comput. Meth. Appl. Mech. Engng. 139, 3–47.

Borja, R.I., 2000. A finite element model for strain localization analysis of strongly discontinuous fields based on standard Galerkin approximation. Comput. Meth. Appl. Mech. Engng. 190, 1529–1549.

Borja, R.I., Regueiro, R.A., 2001. Strain localization in frictional materials exhibiting displacement jumps. Comput. Meth. Appl. Mech. Engng. 191, 2555-2580.

de Borst, R., Sluys, L.J., 1991. Localisation in a Cosserat continuum under static and dynamic loading conditions.. Comput. Meth. Appl. Mech. Engng. 90, 805–827.

de Borst, R., Pamin, J., 1996. Some novel developments in finite element procedures for gradient-dependent plasticity. Int. J. Numer. Meth. Engng. 39, 2477–2505.

Cosserat, E., Cosserat, F., 1909. Théorie des Corps Déformables. Librairie Scientifique A. Hermann et Fils, Paris.

DiGiovanni, A.A., Fredrich, J.T., Holcomb, D.J., Olsson, W.A., 2000. Micromechanics of compaction in an analogue reservoir sandstone. In: Proceedings of fourth North American Rock Mechanics Symposium, Seattle, WA.

Drucker, D.C., Prager, W., 1952. Soil mechanics and plastic analysis or limit design. Q. Appl. Math. 10, 157–165.

Enger, W.M. (Rear Admiral), 1971. Design Manual: Soil Mechanics, Foundations, and Earth Structures. NAVFAC DM-7.

Fredrich, J.T., 1999. 3D imaging of porous media using laser scanning confocal microscopy with application to microscale transport processes. Phys. Chem. Earth 24, 551–561.

Garikipati, K.R., Hughes, T.J.R., 1998. A study of strain localization in a multiple scale framework – the one dimensional problem. Comput. Meth. Appl. Mech. Engng. 159, 193–222.

Garikipati, K., Hughes, T.J.R., 2000a. A variational multiscale approach to strain localization – formulation for multidimensional problems. Comput. Meth. Appl. Mech. Engng. 188, 39–60.

Garikipati, K., Hughes, T.J.R., 2000b. Embedding a micromechanical law in the continuum formulation – a multiscale approach applied to discontinuous solutions. Int. J. Computat. Civil Struct. Engng., submitted for publication.

Holcomb, D.J., Costin, L.S., 1986. Detecting damage surfaces in brittle materials using acoustic emissions. J. Appl. Mech. 108, 536–544.

Hughes, T.J.R., 1980. Generalization of selective integration procedures to anisotropic and nonlinear media. Int. J. Numer. Meth. Engng. 15, 1413–1418.

Hughes, T.J.R., 1987. The Finite Element Method. Prentice-Hall, N.J.

Hughes, T.J.R., 1995. Multiscale phenomena: Green's functions, the Dirichlet-to-Neumann formulation, subgrid scale models, bubbles and the origins of stabilized methods. Comput. Meth. Appl. Mech. Engng. 127, 387–401.

Hughes, T.J.R., Feijóo, G.R., Mazzei, L., Quincy, J.-B., 1998. The variational multiscale method – a paradigm for computational mechanics. Comput. Meth. Appl. Mech. Engng. 166, 3–24.

Janbu, N., 1954. Stability analysis of slopes with dimensionless parameters. Harvard University Harv. Soil Mech. Ser. 46, 1–81.

Liu, W.K., Hao, S., Belytschko, T., Li, S., Chang, C.T., 1999. Multiple scale meshfree methods for damage fracture and localization. Comput. Mater. Sci. 16, 197–205.

Loret, B., Prevost, J.H., 1990. Dynamic strain localization in elasto-(visco)-plastic solids. Part 1. General formulation and one-dimensional examples. Comput. Meth. Appl. Mech. Engng. 83, 247– 273.

Lubliner, J., 1990. Plasticity Theory. Macmillan, New York.

Matthies, H., Strang, G., Christiansen, E., 1979. The saddle point of a differential program. In: Glowinski, R., Rodin, E.Y., Zienkiewicz, O.C. (Eds.), Energy Methods in Finite Element Analysis. Wiley, New York, pp. 309–318.

Mindlin, R.D., 1963. Influence of couple-stresses on stress concentrations. Exper. Mech. 3, 1–7.

Needleman, A., 1988. Material rate dependence and mesh sensitivity in localization problems. Comput. Meth. Appl. Mech. Engng. 67, 69–85.

Oliver, J., Cervera, M., Manzoli, O., 1999. Strong discontinuities and continuum plasticity models: the strong discontinuity approach. Int. J. Plast. 15, 319–351.

Ortiz, M., Leroy, I., Needleman, A., 1987. A finite element method for localized failure analysis. Comput. Meth. Appl. Mech. Engng. 61, 189–214.

Ord, A., Vardoulakis, I., Kajewski, R., 1991. Shear band formation in Gosford sandstone. Int. J. Rock Min. Sci. Geomech. Abstr. 28, 397–409.

Prevost, J.H., Höeg, K., 1975. Soil mechanics and plasticity analysis of strain softening. Géotechnique 25, 279–297.

Ramaswamy, S., Aravas, N., 1998a. Finite element implementation of gradient plasticity models. Part I. Gradient-dependent yield functions. Comput. Meth. Appl. Mech. Engng. 163, 11–32.

Ramaswamy, S., Aravas, N., 1998b. Finite element implementation of gradient plasticity models. Part II. Gradient-dependent evolution equations. Comput. Methods Appl. Mech. Engng. 163, 33–53.

Regueiro, R.A., 1998. Finite element analysis of strain localization in geomaterials taking a strong discontinuity approach. Ph.D. Thesis, Stanford University.

Regueiro, R.A., Lai, T.Y., Borja, R.I., 1998. Computational modeling of strain localization in soft rock. In: Evangelista, A., Picarelli (Eds.), The Geotechnics of Hard Soils – Soft Rocks. A.A. Balkema, Rotterdam, pp. 789–797.

Regueiro, R.A., Borja, R.I., 1999. A finite element model of localized deformation in frictional materials taking a strong discontinuity approach. Finite Elem. Anal. Des. 33, 283–315.

Rice, J.R., 1971. Inelastic constitutive relations for solids: an internal-variable theory and its application to metal plasticity. J. Mech. Phys. Solids 19, 433–455.

Rudnicki, J.W., Rice, J.R., 1975. Conditions for the localization of deformation in pressure-sensitive dilatant materials. J. Mech. Phys. Solids 23, 371–394.

Runesson, K., Ottosen, N.S., Perić, 1991. Discontinuous bifurcations of elastic–plastic solutions at plane stress and plane strain. Int. J. Plast. 7, 99–121.

Sandler, I.S., Wright, J.P., 1984. Strain-softening. In: Nemat-Nasser, S., Asaro, R., Hegemier, G. (Eds.), Theoretical Foundations for Large Scale Computations of Nonlinear Material Behavior. Martinus Nijhoff, Netherlands, pp. 285–315.

Schaeffer, D.G., 1990. Instability and ill-posedness in the deformation of granular materials. Int. J. Numer. Anal. Meth. Geomech. 14, 253–278.

Simo, J.C., Rifai, M.S., 1990. A class of mixed assumed strain methods and the method of incompatible modes. Int. J. Numer. Meth. Engng. 29, 1595–1638.

Simo, J.C., Oliver, J., Armero, F., 1993. An analysis of strong discontinuities induced by strain-softening in rate-independent inelastic solids. Comput. Mech. 12, 277–296.

Simo, J.C., Oliver, J., 1994. A new approach to the analysis and simulation of strain softening in solids. In: Bažant, Z.P., Bittnar, Z., Jirásek, M., Mazars, J. (Eds.), Fracture and Damage in Quasibrittle Structures. E&FN Spon, London, pp. 25–39.

Simo, J.C., Hughes, T.J.R., 1998. Computational Inelasticity. Springer, Berlin.

Stakgold, I., 1998. Green's Functions and Boundary Value Problems, second ed. Wiley, New York.

Taylor, R.L., Simo, J.C., Zienkiewicz, O.C., Chan, A.C.H., 1986. The patch test–A condition for assessing FEM convergence. Int. J. Numer. Meth. Engng. 22, 39–62.

Vardoulakis, I., Goldschieder, M., Gudehus, G., 1978. Formation of shear bands in sand bodies as a bifurcation problem. Int. J. Numer. Anal. Meth. Geomech. 2, 99–128.

Vermeer, P.A., de Borst, R., 1984. Non-associated plasticity for soils, concrete, and rock. Heron 29, 3–64.

Wan, R.G., Chan, D.H., Morgenstern, N.R., 1990. A finite element method for the analysis of shear bands in geomaterials. Finite Elem. Anal. Des. 7, 129–143.